Chemical Geology 568 (2021) 120142

Contents lists available at ScienceDirect

Chemical Geology

journal homepage: www.elsevier.com/locate/chemgeo

Lithium and potassium isotope fractionation during silicate rock dissolution: An experimental approach

Wenshuai Li [a,*], Xiao-Ming Liu [a,*], Kun Wang [b], Piers Koefoed [b]

[a] Department of Geological Sciences, University of North Carolina-, Chapel Hill, NC 27599-3315, USA
[b] Department of Earth and Planetary Sciences and McDonnell Center for the Space Sciences, Washington University in St. Louis, MO 63130, USA

ARTICLE INFO

Editor: Dr Don Porcelli

Keywords:
Silicate rocks
Chemical weathering
Dissolution
Lithium
Potassium
Isotope

ABSTRACT

This study experimentally investigates the isotopic behaviors of Li and K during the dissolution of silicate rocks (i.e., basalt and granite). Proton-driven dissolution (in 0.8 M HNO_3) and ligand-driven dissolution (in 5 mM critic acid or oxalic acid) experiments were performed in batch-closed systems over 15 days. We provide a time-series interpretation of Li and K isotope fractionation during silicate dissolution in ultra-acidic (unidirectional) and near-natural (biologically affected) environments. As the reaction progressed, we measured large isotope fractionation between the liquid (l) phase and the pristine silicate (s) phase, ranging from −10.3 to 0.1‰ ($\Delta^7Li_{l\text{-}s}$) and from −1.01 to −0.11‰ ($\Delta^{41}K_{l\text{-}s}$) through the early stage of dissolution (<24 h). The enrichment of lighter Li and K isotopes in the solutions rapidly diminished as rock dissolution continued and gradually approached equilibrium to the end of experiments. In contrast, resorption of pre-leached isotopically lighter Li on silicate residuals during ligand-driven dissolution produced lighter isotope enrichment in the solutions compared to the initial rock by up to 2.8‰. Despite the preferential dissolution of specific minerals, the isotope fractionation patterns of Li and K do not vary with lithology, indicating limited inter-mineral isotopic differences. During the experiments, the Li and K isotopic pattern could be divided into two-to-three stages. The initial enrichment of light isotopes in the liquids can be ascribed to the kinetic isotope effect, confounded by diffusion and ion solvation. A later transition towards no isotope fractionation of Li and K may be explained by (i) the masking effect from dissolution, and (ii) an imprint from the destruction of $^7Li/^{41}K$-enriched surface layers. Lateral resorption of solute Li after ~100 h reaction could be facilitated by the electrostatic attraction from increasing surface negative charges and active hydroxyls with increasing pH during ligand-driven dissolution (pH ~ 4) relative to proton-driven dissolution (pH ~ 0.2). Therefore, the presence of organic ligands impacts dissolution stoichiometry, and potentially modifies Li isotope fractionation in natural weathering environments. In comparison, K isotope fractionation driven by rock dissolution stops immediately (within days) after starting the experiments. This research helps to understand the mechanisms of Li and K isotope fractionation during chemical weathering and trace long-term climate change using geological records.

1. Introduction

Chemical weathering is one of the key drivers of crustal evolution on Earth (Goldich, 1938). Chemical weathering shapes Earth's surface, modulates nutrient supplies from land to ocean, and regulates the long-term carbon cycle and habitability over geologic timescale (Gaillardet et al., 1999; Amiotte Suchet et al., 2003; Hartmann et al., 2013; Eiriksdottir et al., 2015). Continental-marine elemental inventories and associated isotope fractionation help with the reconstruction of chemical weathering processes (Edmond, 1992; De La Rocha and DePaolo, 2000; Bayon et al., 2009; Misra and Froelich, 2012; Li et al., 2020a, 2020b), advancing the understanding of climate change. Hence, assessing the mechanics and contribution of chemical weathering to carbon cycles and oxygenation shifts in the atmosphere, hydrosphere, lithosphere, and biosphere have received extensive attention (Stallard, 1995; Henderson, 2002; Holland, 2005; Misra and Froelich, 2012; Bataille et al., 2017; Li and Liu, 2020a). Thus, constraining the intensity (the degree of alteration in weathered materials) and rate (i.e., the mass of change in weathered materials per unit time) of chemical weathering using geochemical proxies, such as stable isotope ratios of $^7Li/^6Li$ and

* Corresponding authors.
E-mail addresses: wenshuai@live.unc.edu (W. Li), xiaomliu@unc.edu (X.-M. Liu).

https://doi.org/10.1016/j.chemgeo.2021.120142
Received 3 August 2020; Received in revised form 20 November 2020; Accepted 21 February 2021
Available online 24 February 2021

$^{39}K/^{41}K$, have been investigated extensively (Dellinger et al., 2015; Tomascak et al., 2016; Li et al., 2019a; Chen et al., 2020; Li and Liu, 2020b; Teng et al., 2020; Wang et al., 2021). In the case of highly mobile Li and K during continental weathering, the primary influx of Li and K to the marine systems is produced from silicate dissolution (e.g., Huh et al., 1998; Liu and Rudnick, 2011; Li et al., 2019a; Wang et al., 2021). Therefore, understanding the controlling factors of isotope fractionation of Li and K (i.e., direction, magnitude and mechanism) during silicate dissolution is significant when applying them as tracers of continental weathering.

Commonly, chemical weathering can be conceptually divided into two possible processes generating isotope fractionation: (i) rock dissolution and (ii) soil (and secondary mineral) formation. So far, experimental silicate rock leaching has been shown to exhibit negligible Li isotope fractionation (e.g., Pistiner and Henderson, 2003; Millot et al., 2010; Wimpenny et al., 2010). Therefore, the utilization of Li isotopic signals to trace weathering is mostly linked to the preferential scavenging of isotopically lighter Li in secondary minerals during adsorption and incorporation, based on both field observations (e.g., Huh et al., 2001; Kisakurek et al., 2005; Pogge von Strandmann and Henderson, 2015; Henchiri et al., 2016; Murphy et al., 2019; Li et al., 2020a, 2020b; Ma et al., 2020)' and laboratory experiments (e.g., Williams and Hervig, 2005; Vigier et al., 2008; Wimpenny et al., 2015; Hindshaw et al., 2019; Pogge von Strandmann et al., 2019; Li and Liu, 2020b). By contrast, there is a lack of knowledge of K isotope fractionation during weathering induced by rock dissolution and pedogenesis.This is because high-precision K isotope measurements (2SD ~ 0.1‰) have only become possible due to recent improvements in the analytical method (e.g., Li et al., 2016; Wang and Jacobsen, 2016; Morgan et al., 2018; Hu et al., 2018; Chen et al., 2019). So, the impact of silicate dissolution on K isotope behavior remains elusive, requiring further constrains.

Dissolution impacts on Li and K isotope fractionation might be more complicated than previous expectations. For example, the kinetic isotope effect likely exerts additional impacts on Li isotope fractionation during silicate dissolution before reaching equilibrium, as ^{6}Li diffuses faster than ^{7}Li in liquids (Bourg et al., 2010; Hofmann et al., 2012). A similar effect was observed in experimental studies that recorded the preferential release of ^{6}Li from minerals into solution at the starting period of forsterite/basalt alteration in through-flow reactors (Wimpenny et al., 2010) and batched systems (Verney-Carron et al., 2011). The signal of kinetic effects might be overprinted by successive isotopic equilibrium after reaching the steady state. Likewise, such a kinetic-to-equilibrium transition trend has been found in multiple metal isotope systems during proton-driven and ligand-driven dissolution (Fe: Brantley et al., 2004; Wiederhold et al., 2006; Kiczka et al., 2010a; Zn: Weiss et al., 2014; Cu: Wall et al., 2011; Mg: Ryu et al., 2011). Exceptions could be attributed to the dependence on the primary mineralogy of silicates (Mo: Voegelin et al., 2012), dissolution congruency (Mg: Balland-Bolou-Bi et al., 2019), oxidative dissolution (Cu: Kimball et al., 2010; Fernandez and Borrok, 2009), ligand-ion complexation (Fe, Chapman et al., 2009; Kiczka et al., 2010b),backward reaction (Li, Wimpenny et al., 2010), and the persistent isotopic equilibrium through reactions (Sr: Mavromatis et al., 2017; Ba: Mavromatis et al., 2016). Hence, a systematic investigation is required to achieve an in-depth understanding of Li and K isotope fractionation during rock dissolution, with leaching experiments under constrained settings being suitable. Since Li and K are chemically comparable (e.g., redox-insensitive and free ionic phases in water), we hypothesize that Li and K isotopes should behave similarly during dissolution and be undiscernible to organic ligands.

The objective of this study is to investigate the direction and magnitude of Li and K isotope fractionation via the dissolution of igneous rocks in time-series. Basalt and granite are the most common exposed silicate rocks, meaning they can provide critical information on chemical weathering in Earth's surficial environments. The combination of dissolution stoichiometry, and Li and K isotope data potentially provides novel insights into the significance and mechanisms of unidirectional dissolution (ultra-acidic settings prepared by 0.8 M HNO_3) and the impact of organic acids (natural analogy) on Li and K isotopic behavior during rock dissolution. By sampling supernatants at different time intervals, we determined the isotopic variations of Li and K from source rock signals at far-from-equilibrium (chemical) conditions, close-to-equilibrium (chemical) conditions, and possible back-reaction in isotope disequilibrium. In this paper, the term "chemical equilibrium" represents the equilibrium of the elements between the solid and fluid phases irrespective of their isotopic signals. A far-from-equilibrium state to a close-to-equilibrium state refers to the approach to equal forward and reverse reactions, i.e., negligible overall reaction. The term "isotope equilibrium" stands for the equilibrium distribution of isotopes between the solid and the fluid phases based on the stable isotope theory (Schauble, 2004). The change of kinetic fractionation to equilibrium fractionation refers to a change from unidirectional isotope fractionation to a partial separation of isotopes between two or more phases in equilibrium. Above definitions are widely used in dissolution systems (Pearce et al., 2012). This study offers direct evidence of dissolution-promoted Li and K isotope fractionation, which is of great interest for future research on chemical weathering.

2. Experimental Setup

2.1. Samples and reagents

Deionized water (MQ, 18.2 MΩ·cm) produced by the Milli-Q Direct-Q 3UV (Millipore™) system was used in all experiments, unless otherwise marked. Double-distilled nitric acid from a Teflon® sub-boiling still system (Savillex™) was diluted using deionized water to the required molarity. Ultrapure-grade oxalic acid and citric acid (hereafter referred to OA and CA as their abbreviations, respectively) were sourced from Fisher Scientific Inc. All polyethylene wares and Teflon® beakers were cleaned with 2 wt% HNO_3 and then rinsed thoroughly using deionized water. Research-grade Hawaiian basalt (BHVO-2) and Colorado granodiorite (GSP-2) standards were obtained from the United States Geological Survey to preclude grain-size effects. In consideration of contamination and initial non-linear reaction kinetics due to fine particles adhered to rocks, labile components were removed through ultrasonic treatment in deionized water, followed by methanol rinses (Kiczka et al., 2010a; Weiss et al., 2014). After cleaning, the concentrations of Li, K, Al and Si in eluents are lower than the detection limits of the quadrupole inductively-coupled-plasma mass spectrometer (Q-ICP-MS). Rock powders were then dried in ambient conditions and stored for future analyses.

2.2. Experiments

To determine the behaviors of Li and K during liberation from silicate frameworks through chemical weathering and their associated isotope fractionation, powdered igneous rocks were subjected to acidic treatment under constrained conditions (e.g., solute pH, reaction time, and temperature). Two individual experimental sets were designed and conducted in batch closed-systems, including (1) proton-driven dissolution of basalt and granite using 0.8 M HNO_3 at 25 or 80 °C; (2) ligand-driven dissolution of basalt and granite using 5 mM CA/OA at 25 °C. We note that prepared 0.8 M HNO_3 was adopted to simulate corrosive environments where backward reactions would be significantly precluded, thus resulting in approximate unidirectional dissolution (Pistiner and Henderson, 2003). Such an ultra-acidic condition (pH ~ 0.2) favors forward dissolution reactions, and exerts strong controls against back-reactions, ensuring liberated cations are isolated in the surrounding solution. In addition to the ambient condition of proton-driven dissolution, a water temperature of 80 °C was applied to simulate basalt-hosted geothermal systems (Olasolo et al., 2016). It is known that the presence of organic acids (or ligands) largely affects mineral dissolution kinetics and stoichiometry (Li and Liu, 2020a). To approximate Earth's

surface conditions with biological interferences (e.g., soils) and maintain consistency with previous studies of ligand-controlled silicate dissolution (Wiederhold et al., 2006; Chapman et al., 2009; Weiss et al., 2014), 5 mM of the organic acids were chosen for the reacted solution. Low- molecular-weight organic acids such as OA and CA are ubiquitous on Earth's surface, normally playing a substantial role in biogeochemical weathering processes (Hausrath et al., 2011). In addition, possible backward processes can also be evaluated in the experiments with organic acids (e.g., Chapman et al., 2009; Weiss et al., 2014) at relatively high pH. Solute pH was not buffered but was routinely monitored using the pH meter at each sampling step. A pH electrode with 3 M NaCl internal electrolyte solutions rather than 3 M KCl was used to avoid any K contamination during pH adjustment and lateral pH measurement. The pH meter (Thermofisher™) was calibrated using the standard pH references (Fisher Scientific™, pH = 4/7/10). As for experiment design, basalt was subjected to more acid treatments than granite to test Li and K isotope behaviors. The main reason for this is basalt weathering is responsible for more than 30% of global CO_2 consumption (Gaillardet et al., 1999), so it needs comprehensive environmental constraints in a dissolution study such as this.

Prior to reaction, approximately 500 ± 0.1 mg rock samples were suspended in borosilicate Erlenmeyer flasks (Corning™) on a thermostatic plate, filled with 250 mL 0.8 M HNO_3 or 5 mM organic acids. Continuous agitation is important during dissolution, affecting solute distribution in solutions and boundary film formations on solids. The size of the reactor was 250 mL, and the solid-to-solution ratio was kept constant at 2.0 g/L. The initial ionic strength of solutions was adjusted to 10 mM using NaCl (K- and Li-free, extra pure). Reactors were kept in atmospheric conditions, and continuously mixed at 550 rpm using magnetic stir bars to ensure efficient solution-rock contact and surface-reaction controlled dissolution (Wimpenny et al., 2010). Through the entire experiment, the dissolution systems changed from far-from-equilibrium to near-equilibrium over a period of 15 days. Periodical sampling of filtered supernatant while manually shaking the reactor was allowed to homogenize the solid-fluid phases. Liquid extracts (~0.5 mL) using syringe samplers were centrifuged and separated from solid residues by 0.22 um cellulose acetate syringe filters (Thermo Fisher Scientific™), then transferred into acid-clean polypropylene tubes. The silicate residues were separated from the liquids at the end of the experiment, rinsed with deionized water, dried, and stored at 4 °C. Each silicate-regent combination was carried out in replicates to ensure data reproducibility and accuracy. Experiment conditions are listed in Tables 2–3.

3. Analytical methods

3.1. Elemental analysis

All chemical pretreatments were performed in a class-100 vented laminar flow workstation (Airclean™, 600 PCR) in the Plasma Mass Spectrometry Lab at the University of North Carolina at Chapel Hill. To complete a compositional description of major elements, solid pellets were measured using X-ray fluorescence (XRF) at ALS Chemex Labs following a $Li_2B_4O_7$ fusion approach. After weighing, both international geostandards and samples were digested using a mixture of concentrated HCl-HNO_3-HF acids at >150 °C, following an approach reported in Li et al. (2019b). Solid and dissolved concentrations of Li, Na, K, Mg, Al, Fe, Ca, Sr, Nb, Si, and Ti were determined using a Q-ICP-MS (Agilent™ 7900) at the University of North Carolina, Chapel Hill. The instrument was calibrated by a series of ICP standard solutions of known concentrations. Internal standards, including Be, Ge, Rh, In, Ir, and Bi were employed for signal drift correction. International references BHVO-2 (basalt), GSP-2 (granodiorite), and JG-2 (granite) were measured in the same batch to ensure analytical accuracy and reproducibility (Table 1). The elemental compositions of international references were certified by the United States Geologic Survey (USGS) and the Geological Survey of Japan (GSJ). During analysis, a precision of <3% (relative standard derivation, RSD) was achieved. The RSD value was calculated based on an average of six analytical cycles of the same sample. The measurement was validated with the results obtained on different reference materials, yielding an accuracy <10% for reported elements (relative to reference certified values), and data are justified from a compilation of inter-laboratory comparisons (Table 1).

3.2. Solid characterization

Mineralogical identification on powdered soils was conducted using X-ray diffraction (XRD) at the University of North Carolina at Chapel Hill. Solid samples were ground into powders with an agate mortar and pestle and smeared on glass slides. X-ray spectra were obtained on an XRD diffractometer (Rigaku™) with Ni-filtered Cu Kα radiation (40 kV, 40 mA) and the scan range from 3° to 65° 2θ with a 0.01° step-size and 10 s acquisition time (Fig. 1). Infrared spectroscopy has advantages in surface sensitivity to acquire information on the alteration level of reacted silicates. Attenuated total reflectance Fourier transform infrared spectroscopy (ATR-FTIR) spectra were measured using the Bruker™ Hyperion 1000 with Tensor 27 spectrometer (Fig. 2). This instrument was equipped with an MCT-A detector and a platinum diamond ATR crystal accessory in order to reach high interface sensitivity. Vacuum-dried solids from different experimental groups were loaded on a plate, and the spectra were collected (256 scans) with a 2 cm^{-1}

Table 1
Elemental and isotopic compositions of basalt and granite standards.

SRM	[Li]	[K]	[Mg]	[Al]	[Ca]	$\delta^7Li_{measured}$	2SD	$\delta^{41}K_{measured}$	2SD
NO.	(ppb)	(ppm)	(ppm)	(ppm)	(ppm)	(‰)	(‰)	(‰)	(‰)
BHVO-2	4550[a]	4224	43,169	72,180	81,220	4.60[a]	1.1	-0.49[a]	0.05
(Basalt,	5000[b]	4314	43,380	71,470	81,428	4.63[i]	0.29	-0.50[m]	0.19
USGS)	4500[c]	4256	43,542	71,152	81,428	4.70[j]	0.57	-0.52[n]	0.24
	n.d.[d]	4200	41,800	68,300	77,600	4.63[k]	0.16	-0.48[o]	n.d.
	4270[e]	4300	43,700	70,900	80,700	4.50[l]	0.24	-0.41[P]	0.02
GSP-2	3590[a]	44,510	5790	79,200	15,400	-0.46[a]	1.1	-0.46[a]	0.09
(Granite,	3600[b]	44,642	5760	78,882	15,000	-0.56[i]	0.55	-0.50[m]	0.12
USGS)	3480[f]	44,200	5900	80,200	16,000	-0.56[j]	0.72	-0.48[n]	0.1
	n.d.[g]	44,800	n.d.	n.d.	15,000	-0.78[l]	0.25	-0.42[P]	0.03
JG-2	46.1[a]	38,956	210	68,525	4960				
(Granite,	42.2[b]	39,080	220	66,010	5000				
GSJ)	n.d.[h]	36,000	n.d.	n.d.	4900				

Note: [a]Data collected in this study; [b]Certified values; [c]Jochum et al. (2016); [d]Zhao and Zheng (2015); [e]Zhang et al. (2016); [f]Zhang et al. (2016); [g]Cotta et al. (2007); [h]Korotev (1996); [i]Li et al. (2019b); [j]Liu and Li (2019); [k]Huang et al. (2010); [l]Lin et al. (2016); [m]Li et al. (2016); [n]Morgan et al. (2018); [o]Chen et al. (2019); [P]Li et al. (2020a). 2SD: two standard deviation corrected by the Student's *t* factor; N: the number of isotope analytical cycles; n.d.: not determined.

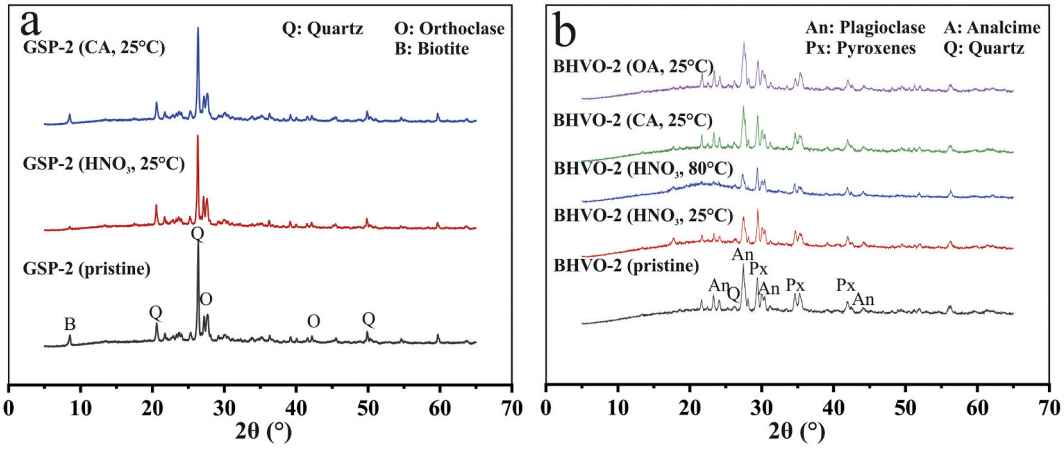

Fig. 1. Normalized XRD spectra of reacted (a) granite and (b) basalt during proton-driven and ligand-driven dissolution. Abbreviations: OA: oxalic acid; CA: citric acid; Q: quartz; O: orthoclase; B: biotite; An: plagioclase; Px: pyroxenes; A: analcime. There are measurable changes in mineral-specific peaks before and after reactions, revealing heterogeneous dissolution (or selective dissolution of some mineral phases).

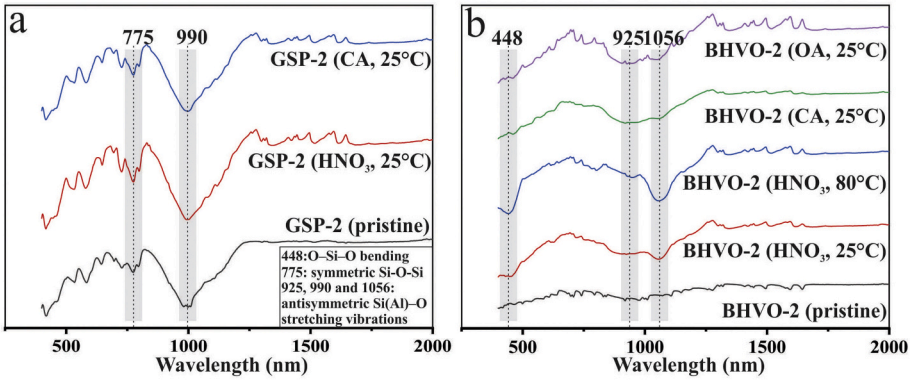

Fig. 2. Measured ATR-FTIR spectra for reacted silicate rocks after dissolution reactions of (a) granite and (b) basalt. Variations in the band at 925/990 cm^{-1} and 1056 cm^{-1} suggest the breakdown of SiO_3 groups and Si-O-Si framework by proton-driven and ligand-driven dissolution (Yin et al., 2010). The changes in the band vibration conform to the dissolution stoichiometry determined in our study (Tables. 2-3), which imply more intensive alteration of the silicate rock skeleton at lower pH (0.8 M HNO_3) and/or higher temperature (80 °C).

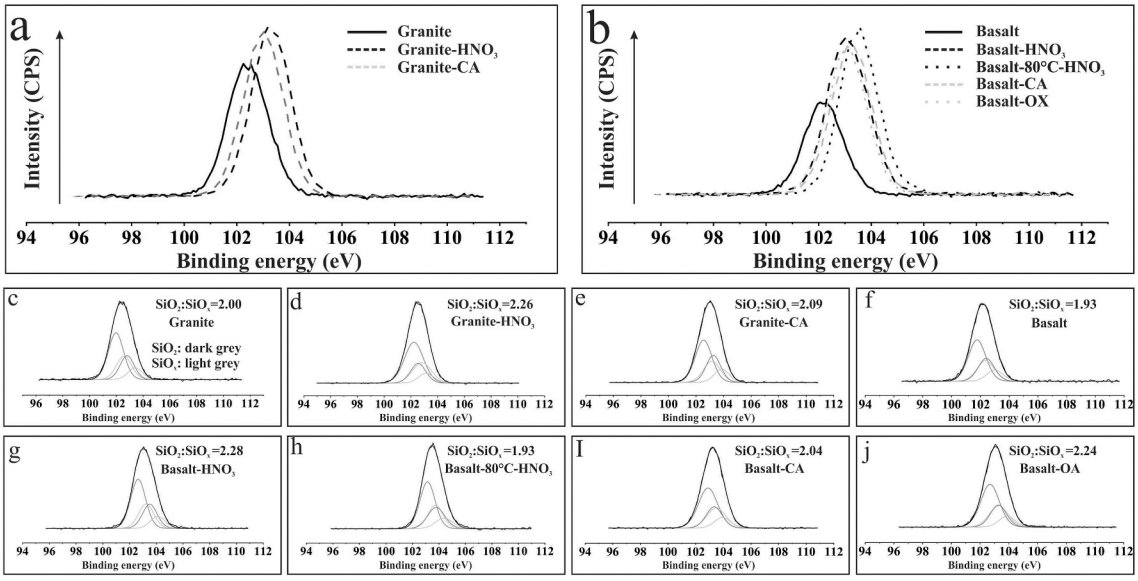

Fig. 3. Fitted high-resolution Si 2p XPS peaks of pristine silicate rocks (basalt and granite) and reacted solids. Only SiO_x ($x > 2$) in the high bonding energy region of ~103–104 eV and SiO_2 in the low high bonding region of ~102–103 eV can be identified without polymeric Si. In the plots (a-b), Si XPS spectra of pristine (solid lines) and reacted rocks (dashed lines) in proton-driven (black lines) and ligand-driven experiments (grey lines) are displayed. In the plots (c-j), the original spectra of rocks (envelops) are marked using black solid lines, and the doublets of two Si species (SiO_2 and SiO_X ($x > 2$)) are marked by grey solid lines. The ratio of SiO_2/SiO_x over 2.00 (unreacted granite) or 1.93 (unreacted basalt) implies the development of amorphous silica layer on the surface of reacted rocks (i.e., leached layer).

resolution and background subtraction.

Surface silica phases were characterized by X-ray photoelectron spectroscopy (XPS). The high-resolution scans of Si_{2p} XPS with fittings are shown in Fig. 3. The survey scans were collected over a range of binding energy (BE) from 0 to 1100 eV with a step size of 700 meV and dwell time of 75 ms. A narrower binding energy range and step size were applied to acquire higher resolution scans of Si atoms, with a range of 96–112 eV, with 0.25 eV step size and 100 ms dwell time, and processed with CASAXPS.

3.3. Chromatography

All isotope pretreatments were performed in a class-100 vented laminar flow workstation (Airclean™, 600 PCR) in the Plasma Mass Spectrometry Lab at the University of North Carolina at Chapel Hill. An aliquot of the digested samples was evaporated to dryness and re-fluxed by 2 mL 0.7 M HNO_3 prior to loading onto columns. Lithium and potassium fractions were obtained after column purification, following the two-step approach modified from Liu and Li (2019) and Chen et al. (2019). The first column was packed with 17 mL AG50-X8 cation-exchange resin (200–400 mesh, Bio-Rad™), and conditioned in 0.7 M HNO_3. The first Li fraction was collected with Na before most of the matrix elements being eluted, and the first K fraction was collected with Rb after Li was eluted. Collected elution cuts were evaporated to dryness on a hotplate and re-dissolved in 1 mL 0.2 M HCl for the second Li column and 1 mL 0.5 M HNO_3 for the second K column, respectively. The setup of the second Li and K columns were identical to the first except for volume and inner diameter. The second Li fraction was collected after other matrix elements (namely Na) were eluted, with a third (identical) column purification done if necessary (if Li/Na < 0.1). The second K fraction was collected after rest of the matrix elements (namely Rb) were eluted and a third (identical) column separation was performed if needed. After the chromatographic process, the pre-cuts and post-cuts of column chemistry (fractions recovered before and after K-collecting volumes) were checked for Li, K, Na, Al, Fe, Rb, and Ti on the Agilent™ 7900 Q-ICP-MS, to guarantee satisfactory Li and K yields (~100%) and low matrix contents, ensuring the reliability of isotope analyses by Q (MC)-ICP-MS (Chen et al., 2019; Liu and Li, 2019).

3.4. Isotope analysis

Procedural blanks (10 mM NaCl) were monitored for experiment runs (≤0.01 ng Li), which were negligible in comparison to collected Li fractions of natural and laboratory samples at μg-levels. The Li isotope analysis was performed using the same Q-ICP-MS instrument as the elemental analysis and the detail was previously reported in Liu and Li (2019). Prior to measurement, samples and standards were matrix matched to a concentration of 0.5 ppb Li in 2% HNO_3. We adopted a microflow self-aspirating (Agilent™, 200 $\mu L \cdot min^{-1}$) PFA nebulizer, quartz spray chamber, quartz torch, and 2.5 mm internal diameter injector. To reach high signal stability and low background, we optimized the carrier gas flow (0.95 $L \cdot min^{-1}$) and the make-up gas flow (0.35 $L \cdot min^{-1}$). The instrumental sensitivity was about 250,000 cps on ^7Li for 0.5 $\mu g \cdot L^{-1}$ solution. Because of the low sample concentration (0.5 ppb Li), a long washing time (180 s) was used during sample transition to maintain low background signals and control memory effects. The sample-standard bracketing method (7 cycles) was used, and concentration matching between standards and samples was limited to >95%. Since the NIST L-SVEC is no longer available and the IRMM−016 standard has an identical Li isotopic composition, and the IRMM-016 standard was used here. The Li isotopic composition is expressed as δ^7Li, the per mil deviation from the IRMM-016 standard ratio:

$$\delta^7Li_{sample}\ (‰) = \left\{ \frac{\left(^7Li/^6Li\right)_{sample}}{\left(^7Li/^6Li\right)_{IRMM-016}} - 1 \right\} \times 1000 \quad (1)$$

The USGS granite (GSP-2) and basalt (BHVO-2) standards were analyzed along with samples for quality control, and the Li isotope values fall within the uncertainties of previously reported data (Table 1). Net Li isotope fractionation between dissolved Li and Li hosted in the rocks, Δ^7Li was calculated using the following equation:

$$\Delta^7Li_{l-s} = \delta^7Li_{liquid} - \delta^7Li_{pristine\ solid} \quad (2)$$

The long-term external precision is 1.1‰, derived from the 2SD of 1-year repeat analyses of IRMM-016 and standard igneous rock references JG-2 and BCR-2 (Liu and Li, 2019).

Procedural K blanks were monitored for experiment runs (≤10 ng K), which were negligible in comparison to collected K fractions of natural and laboratory samples at μg−/mg-levels. Purified K solutions were introduced into a Neptune Plus MC-ICPMS (Thermo Scientific™) at the Isotope Cosmochemistry Laboratory, Washington University in St. Louis. Here, we employed the cold plasma technique to residual and isobaric ($^{40}Ar^1H^+$ on $^{41}K^+$ and $^{38}Ar^1H^+$ on $^{39}K^+$) argides (Chen et al., 2019). In addition to monitoring of ^{41}K and ^{39}K, we measured $^{40}Ar(^{40}Ca)$ and ^{44}Ca to account for interferences and/or contamination. Samples were introduced into the instrument through an Elemental Scientific™ APEX omega, equipped with a desolvation membrane to improve sensitivity and reduce the generation of hydride and oxide. A sample-standard bracketing technique (>6 cycles) was used with the K NIST SRM 3141a standard to correct instrumental mass bias. Instrumentation and analytical details are documented in Chen et al. (2019). Sample isotopic composition is reported in a δ-notation, as the per mil (‰) deviation from the K NIST SRM 3141a isotope standard:

$$\delta^{41}K_{sample}\ (‰) = \left\{ \frac{\left(^{41}K/^{39}K\right)_{sample}}{\left(^{41}K/^{39}K\right)_{NIST\ SRM\ 3141a}} - 1 \right\} \times 1000 \quad (3)$$

A long-term reproducibility from replicate analyses of a suite of international references is better than 0.11‰ (2SD) (Chen et al., 2019). The granite (GSP-2) and basalt (BHVO-2) USGS standards were analyzed for quality control, and the isotope values fall within the uncertainty of previously reported data (Table 1). Net K isotope fractionation between dissolved K and K hosted in pristine rocks, $\Delta^{41}K$ was defined by the following equation:

$$\Delta^{41}K_{l-s} = \delta^{41}K_{liquid} - \delta^{41}K_{pristine\ solid} \quad (4)$$

The two standard deviations (2SD) and 95% confidential interval (95%c.i.) provided in Tables and in figures were calculated from 7 to 11 replicates of $\delta^{41}K$ measurement of each sample. Estimated uncertainty on isotopes was propagated based on following equation:

$$\Delta E = \sqrt{(c_1\Delta W_1)^2 + (c_2\Delta W_2)^2 + \ldots + (c_n\Delta W_n)^2} \quad (5)$$

where ΔE is an absolute error, c is a multiplicative factor, and W is additive function inputs.

4. Results

4.1. Solid characterization

X-ray diffractogram displays variations in the intensity of mineral-specific peaks in reacted and pristine rocks (Fig. 1). The order of the decrease in the intensities of mineral-specific peaks is proton-driven dissolution (HNO_3, 80 °C) > proton-driven dissolution (HNO_3, 25 °C) > ligand-driven dissolution (OA and CA, 25 °C). The apparent decreases in ~8^0 and ~ 27^0 (2θ) in the spectra implies the preferential dissolution of mica and feldspar minerals. Based on XRD spectra, there is no evidence in support of secondary phase precipitation. ATR-FTIR spectra reveal vibrations in the bonds between O, Si and Al atoms, in particular for proton-driven dissolution (Fig. 2). Spectra bands at 925/990 cm^{-1} and 1056 cm^{-1} represent the stretching vibrations of the SiO_3 groups

and the bending (Si–O_b–Si) (Yin et al., 2010). There is no detectable infrared signal of secondary minerals on solids from both systems. The high-resolution scans of Si_{2p} XPS with the least R square (best fits to the data) are illustrated in Fig. 3, which mainly consist of two sets of peaks (spin-orbit split doublets with a spacing of 0.62 eV, $Si_{2p1/2}$ and $Si_{2p3/2}$, Sutherland et al., 1992), offering more information of surface Si alteration during silicate dissolution. The ratios of SiO_2/SiO_x of pristine basalt and granite are 1.93 and 2.00, respectively. After the reaction, SiO_2/SiO_x ratios increase to 2.26 (proton-driven) and 2.09 (ligand-driven) for granite at 25 °C. The SiO_2/SiO_x ratios increase to 2.28 (proton-driven) and 2.04–2.24 (ligand-driven) for basalt at 25 °C, while keeping consistent with the original value of 1.93 during proton-driven dissolution at 80 °C.

4.2. Silicate dissolution

Dissolution kinetics and solute pH of leachates are shown in Fig. 4 and summarized in Tables 2–3. During proton-driven dissolution in 0.8 M HNO_3 at 25/80 °C, solute pH raised by ~0.05, and remained near-constant at ~0.2, with a deviation of <0.1 over the course of basalt and granite experiments. As for ligand-driven dissolution in 5 mM OA/CA at 25 °C, solute pH increased from 2 to 4 within the first 24 h of the reaction, and reached a plateau of ~4.5 during the late stage of experiments (>24 h) (Fig. 4a–b). The release of Li and K mostly followed a parabolic pattern as solute pH evolved in both dissolution systems. At the early dissolution stage <24 h, rapid accumulation of Li and K in leachates occurred, followed by retarded dissolution >24 h in both proton-driven and ligand-driven dissolution systems dependent on the distance from equilibrium. During the late stage of ligand-driven dissolution, dissolved Li concentrations decreased after ~100 h of reaction (Fig. 4c–f). By the end of the experiment (15 days), 29.6–79.2 wt% rock-hosted Li was liberated during proton-driven dissolution, and 1.9–20.1 wt% Li was liberated by ligand-driven dissolution. In comparison, 22.5–56.3 wt% primary K was released during proton-driven dissolution, whereas only 4.2–14.5 wt% K was liberated during ligand-driven dissolution. The kinetics of dissolution can be visually divided into two to three successive stages: (I) steep, incipient leaching far from equilibrium (<24 h), followed by (II) a mild, prolonged steady-state stage approaching chemical equilibrium after 24 h, or (III) with an intermediate, backward state. Dissolution stoichiometry is shown in Fig. 5 and provided in Tables 2–3. The stoichiometry of ion liberation exhibits differences between proton-driven and ligand-driven dissolution systems. Linear correlations can be found in proton-driven dissolution, and element ratios (based on ion release fractions of fresh rocks) derived from the 1:1 line (except for a case at 80 °C). In contrast, ligand-driven dissolution produces non-linear stoichiometric patterns.

4.3. Li isotope fractionation

The experiment setup of this study is different from earlier studies (Table S1), which leads to unique isotope patterns. The evolution of Li isotopic compositions in the liquid and the liquid relative to the solid (i.e., expressed as $\Delta^7Li_{l\text{-}s} = \delta^7Li_{liquid} - \delta^7Li_{solid}$) are plotted in Fig. 6, and tabulated in Tables 2–3. Pristine granite has a δ^7Li value of 0.6 ± 1.1‰ and pristine basalt shows a δ^7Li value of 4.6 ± 1.1‰. Both proton-driven and ligand-driven dissolution systems exhibit preferential liberation of light isotopes at the early stage of dissolution of basalt and granite (<24 h). The lowest isotopic values appear at the onset of dissolution (~30 min), with the isotope shifts from the initial rock signal being reduced or revered as the reaction proceeded. In proton-driven dissolution, silicates in strongly acidic settings (0.8 M HNO_3) produced dissolved phases depleted in ^{7}Li with δ^7Li of −4.7‰ (for granite) after 14 wt% Li leached and δ^7Li of −4.2‰ (for basalt) after ~4 wt% Li removed at 25 °C; and δ^7Li of −4.0‰ (basalt) after nearly 4 wt% Li leached out at 80 °C at the start of reaction (~30 min). While allowing for some deviations, dissolved phases progressively reached values almost equal to the pristine δ^7Li signals through early to late dissolution stages. Dissolved $\Delta^7Li_{l\text{-}s}$ ranges from −1.0‰ to −2.7‰ at 25 °C after ~79 wt% Li in granite and ~ 30 wt% Li in basalt leached from silicate skeletons and reaches ~0‰ at 80 °C after removing 66 wt% Li from basalt. In ligand-driven dissolution, weak organic acid treatments yielded both isotopically light and heavy Li signatures in dissolved phases. Solute δ^7Li is −4.5‰ for granite after 9 wt% Li removed and − 0.4‰ for basalt after 4 wt% Li removed in CA, and − 5.7‰ for basalt after 21 wt% Li leached in OA at the starting point of dissolution (~30 min). Initial enrichment of lighter Li isotopes in solutions is followed by a transition towards heavier Li isotopic composition compared to the starting δ^7Li. Aqueous $\Delta^7Li_{l\text{-}s}$ values range of 2.8‰ to 0.4‰ after 18 wt% Li for granite and 2 wt% Li for basalt leached from silicate skeleton with CA, and − 2.2‰ after 20 wt% Li for basalt leached in 5 mM OA.

4.4. K isotope fractionation

The evolution of K isotopic signals in the liquid and the liquid

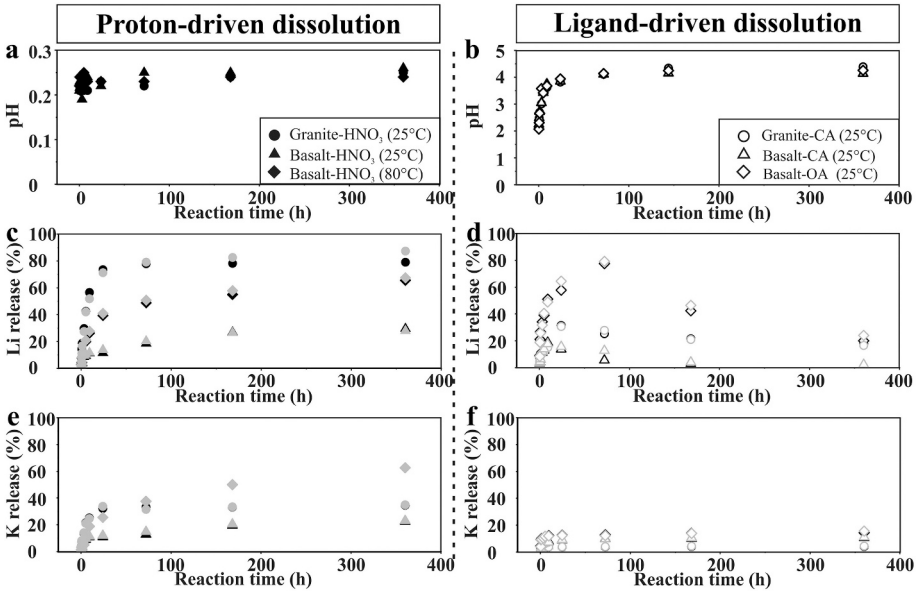

Fig. 4. Characterization of aqueous chemistry as a function of reaction time during proton-driven (solid symbols) and ligand-driven (hollow symbols) dissolution. Experiments were conducted in duplicate (black: $EXP_{(1)}$; grey: $EXP_{(2)}$). (a-b) solute pH vs. reaction time; (c-d) Li release (wt%, the percentage of starting solid Li being liberated into solutions); (e-f) K release (wt%, the percentage of starting solid K being liberated into solutions). Note that the most significant changes in water chemistry occurred at ~24 h in both dissolution sets.

Table 2
Kinetic parameters of silicate rock dissolution during proton-driven dissolution.

Sample	Temp. (°C)	Time	pH	Solute chemistry ($EXP_{(1)}$)								Solute chemistry ($EXP_{(2)}$)		
				δ^7Li (‰)	2SD (‰)	δ^{41}K (‰)	95%c.i. (‰)	N	Released Li (%)	Released K (%)	Released Si (%)	Released Li (%)	Released K (%)	Released Si (%)
Granite (GSP-2) 0.8 M HNO_3	25	10 min	0.21	n.d.	1.1	n.d.	n.d.	n.d.	7.6	4.3	2.6	8.1	4.6	2.7
		30 min	0.22	−4.7	1.1	−0.99	0.04	11	14.3	8.0	6.3	11.2	8.1	5.8
		1 h	0.24	−4.6	1.1	n.d.	n.d.	n.d.	18.8	7.0	8.5	16.7	6.6	6.7
		3 h	0.22	−2.6	1.1	−0.90	0.06	7	29.7	13.8	12.9	27.6	14.1	13.2
		5 h	0.21	−2.2	1.1	n.d.	n.d.	n.d.	42.5	21.5	20.7	42.1	21.2	21.6
		9 h	0.21	−1.8	1.1	n.d.	n.d.	n.d.	56.7	25.2	26.2	52.0	24.7	27.1
		1d	0.23	−1.8	1.1	−0.58	0.04	8	73.6	32.3	35.2	71.4	33.8	35.5
		3d	0.22	−1.7	1.1	n.d.	n.d.	n.d.	78.1	33.2	36.8	79.2	31.6	37.2
		7d	0.24	−1.5	1.1	−0.44	0.06	11	78.3	33.3	37.2	82.7	33.5	38.2
		15d	0.25	−1.5	1.1	−0.40	0.04	n.d.	79.2	34.7	39.1	87.5	35.0	40.1
Basalt (BHVO-2) 0.8 M HNO_3	25	10 min	0.22	n.d.	1.1	n.d.	n.d.	n.d.	1.2	2.1	0.5	1.6	1.9	0.6
		30 min	0.24	−4.2	1.1	−0.93	0.04	9	3.7	3.1	1.2	3.3	3.0	1.1
		1 h	0.21	−3.6	1.1	n.d.	n.d.	n.d.	4.2	3.6	2.3	4.6	3.9	2.5
		3 h	0.22	−1.3	1.1	−0.52	0.04	7	8.7	7.7	4.6	9.5	7.7	5.2
		5 h	0.25	−0.2	1.1	n.d.	n.d.	n.d.	9.4	9.0	4.9	10.4	9.8	5.7
		9 h	0.23	0.3	1.1	n.d.	n.d.	n.d.	11.5	11.0	5.7	11.8	11.6	6.3
		1d	0.23	1.5	1.1	−0.48	0.04	9	11.6	11.1	6.7	13.9	12.1	6.9
		3d	0.23	2.3	1.1	−0.47	0.04	9	18.6	12.8	8.8	20.4	14.9	9.1
		7d	0.24	2.2	1.1	−0.45	0.04	10	26.9	19.7	16.3	26.6	20.6	16.1
		15d	0.24	1.9	1.1	−0.46	0.05	10	29.6	22.5	17.6	28.1	23.1	18.1
Basalt (BHVO-2) 0.8 M HNO_3	80	10 min	0.21	n.d.	1.1	n.d.	n.d.	n.d.	2.8	2.2	1.7	2.6	1.6	1.6
		30 min	0.23	−4.0	1.1	−1.20	0.06	9	4.4	2.7	2.0	5.1	3.2	1.8
		1 h	0.21	n.d.	1.1	n.d.	n.d.	n.d.	7.7	3.8	3.8	8.7	4.1	3.2
		3 h	0.19	1.5	1.1	−0.93	0.06	9	10.0	4.3	3.3	10.4	5.1	3.3
		5 h	0.22	n.d.	1.1	n.d.	n.d.	n.d.	19.9	9.8	7.8	21.1	11.1	7.8
		9 h	0.24	4.3	1.1	−0.76	0.04	9	26.3	16.6	12.1	27.8	18.9	12.6
		1d	0.22	n.d.	1.1	n.d.	n.d.	n.d.	39.5	22.4	22.7	41.1	25.6	21.7
		3d	0.25	4.5	1.1	−0.56	0.05	10	48.9	32.0	23.7	50.9	37.6	23.7
		7d	0.25	n.d.	1.1	n.d.	n.d.	n.d.	55.1	48.7	27.1	58.0	50.1	27.1
		15d	0.26	4.6	1.1	−0.59	0.04	11	65.7	56.3	34.5	67.6	62.7	34.9

Note 1: Li isotopes were measured using a Q-ICP-MS method (Liu and Li, 2019); K isotopes ere measured using a MC-ICP-MS method (Chen et al., 2019). Experiments were conducted in duplicate and isotope data of $EXP_{(1)}$ were reported.
Note 2: N: the number of isotope analytical cycles. We note that $N = 7$ for Li isotope analysis. 95% c.i.: 95% confidence interval; 2SD: two standard deviation corrected by the Student's *t* factor. Net isotope fractionation $\Delta^7Li_{l\text{-}s}$ and $\Delta^{41}K_{l\text{-}s}$ during dissolution reported in this paper could be calculated by the difference between dissolved isotopic composition (shown in this table) and initial rock isotopic composition. n.d.: not determined. Temp.: temperature.

relative to the solid (i.e., expressed as $\Delta^{41}K_{l\text{-}s} = \delta^7K_{liquid} - \delta^7K_{solid}$) are plotted in Fig. 7, and listed in Tables 2–3. Pristine granite has a δ^{41}K value of −0.46 ± 0.05‰, and pristine basalt shows a δ^{41}K value of −0.40 ± 0.05‰. Both proton-driven and ligand-driven dissolution systems exhibit preferential liberation of lighter isotopes at the early stage of dissolution of basalt and granite (<24 h). The lowest isotopic values occur at the very start of dissolution (~30 min), with the isotope shifts from the initial rock signal being reduced or revered as the reaction proceeded. During proton-driven dissolution, the strong acidic reaction (HNO_3) of silicates yielded dissolved phases depleted in ^{41}K with δ^{41}K of −0.99‰ (for granite) after 8 wt% K removed and δ^{41}K of −0.93‰ (for basalt) after 3 wt% K removed at 25 °C; and δ^{41}K of −1.20‰ (basalt) after 3 wt% K leached out at 80 °C at the very beginning of reaction (about 30 min), compared with pristine silicates (basalt, −0.40 ± 0.05‰; granite, −0.46 ± 0.05‰). Allowing for some deviations, dissolved phases progressively approached values almost identical to the pristine δ^{41}K signals through early to late dissolution stages. Aqueous $\Delta^{41}K_{l\text{-}s}$ ranges from 0.06‰ to −0.06‰ at 25 °C after 35 wt% K in granite and 23 wt% K in basalt leached from the silicate frameworks, and reached −0.19‰ at 80 °C after removing around 56 wt% K in basalt. During ligand-driven dissolution, weak acidic treatment yielded an isotopically light signal in dissolved phases. Solute δ^{41}K is −0.98‰ for granite after 3 wt% K leached and − 0.90‰ for basalt after ~2% K removed at 25 °C, and − 1.41‰ for basalt after ~9 wt% K leached at 25 °C at the starting point of dissolution (~30 min). Following a similar pattern as K in proton-driven dissolution, the δ^{41}K in dissolved phases reached the rock signal while allowing for some scatter by the end of the experiment (15 days) at 25 °C. Aqueous $\Delta^{41}K_{l\text{-}s}$ range from 0.07‰ to

Table 3
Kinetic parameters of silicate rock dissolution during ligand-driven dissolution.

Sample	Temp. (°C)	Time	pH	Solute chemistry ($EXP_{(1)}$)								Solute chemistry ($EXP_{(2)}$)		
				δ^7Li (‰)	2SD (‰)	$\delta^{41}K$ (‰)	95%c.i. (‰)	N	Released Li (%)	Released K (%)	Released Si (%)	Released Li (%)	Released K (%)	Released Si (%)
Granite (GSP-2) 5 mM CA	25	10 min	2.30	n.d.	1.1	n.d.	n.d.	n.d.	7.2	2.0	3.1	5.9	1.6	3.3
		30 min	2.48	−4.5	1.1	−0.98	0.03	9	8.9	2.5	5.5	8.0	2.4	5.0
		1 h	2.69	n.d.	1.1	n.d.	n.d.	n.d.	10.3	3.1	6.2	9.4	3.0	5.7
		3 h	3.01	−4.2	1.1	−0.80	0.06	8	11.5	3.3	7.3	11.0	3.2	7.4
		5 h	3.48	n.d.	1.1	n.d.	n.d.	n.d.	12.7	3.4	7.9	12.2	3.5	7.3
		9 h	3.62	−1.6	1.1	−0.66	0.07	8	15.7	3.7	8.9	15.0	3.7	8.4
		1d	3.82	−0.4	1.1	n.d.	n.d.	n.d.	31.5	3.8	15.3	30.8	3.9	14.3
		3d	4.11	0.4	1.1	−0.58	0.05	8	25.4	3.9	16.2	27.8	4.0	15.7
		7d	4.34	1.4	1.1	−0.53	0.03	8	21.6	4.2	16.8	21.1	4.4	16.2
		15d	4.39	2.3	1.1	−0.39	0.04	11	17.8	4.2	17.4	16.6	4.5	16.8
Basalt (BHVO-2) 5 mM CA	25	10 min	2.25	n.d.	1.1	n.d.	n.d.	n.d.	3.2	0.6	1.1	3.6	2.0	0.9
		30 min	2.49	−0.4	1.1	−0.90	0.04	11	4.3	1.9	1.7	4.5	2.9	2.7
		1 h	2.72	n.d.	1.1	n.d.	n.d.	n.d.	6.3	5.1	3.5	6.4	5.4	3.5
		3 h	3.05	0.2	1.1	−0.75	0.04	9	11.4	6.4	6.7	12.2	6.2	6.2
		5 h	3.43	n.d.	1.1	n.d.	n.d.	n.d.	13.0	6.7	7.3	13.9	6.6	7.6
		9 h	3.75	1.8	1.1	n.d.	n.d.	n.d.	18.9	7.8	9.0	17.7	7.3	8.4
		1d	3.85	3.2	1.1	−0.57	0.04	11	13.8	9.0	11.9	15.7	9.3	11.4
		3d	4.11	4.7	1.1	−0.50	0.05	10	5.6	9.8	12.7	12.8	9.7	12.2
		7d	4.15	4.9	1.1	n.d.	n.d.	n.d.	3.0	10.1	13.2	4.1	10.7	12.9
		15d	4.14	5.0	1.1	−0.47	0.05	10	1.9	10.6	13.9	2.4	11.2	13.4
Basalt (BHVO-2) 5 mM OA	25	10 min	2.07	n.d.	1.1	n.d.	n.d.	n.d.	8.9	4.4	3.0	8.4	4.1	3.1
		30 min	2.31	−5.7	1.1	−1.41	0.04	6	21.1	9.3	9.1	18.9	9.1	8.6
		1 h	2.66	n.d.	1.1	n.d.	n.d.	n.d.	26.8	9.9	11.4	25.9	9.5	12.4
		3 h	3.58	−2.3	1.1	−0.84	0.05	10	34.2	10.1	12.1	31.8	10.6	13.6
		5 h	3.42	n.d.	1.1	n.d.	n.d.	n.d.	39.1	11.5	14.1	40.5	11.7	14.6
		9 h	3.68	0.2	1.1	−0.70	0.03	10	51.1	12.2	18.1	49.0	12.0	18.6
		1d	3.94	n.d.	1.1	−0.53	0.06	8	57.8	12.6	18.9	64.5	12.4	19.9
		3d	4.14	1.3	1.1	−0.51	0.03	9	77.7	12.8	20.9	79.3	12.3	21.9
		7d	4.25	1.9	1.1	−0.56	0.05	11	42.5	14.0	21.3	46.5	13.9	22.3
		15d	4.26	2.4	1.1	−0.45	0.05	10	20.1	14.5	22.1	24.1	15.6	22.5

Note 1: Li isotopes were measured using a Q-ICP-MS method (Liu and Li, 2019); K isotopes ere measured using a MC-ICP-MS method (Chen et al., 2019). Experiments were conducted in duplicate and isotope data of $EXP_{(1)}$ were reported.
Note 2: N: the number of isotope analytical cycles. We note that N = 7 for Li isotope analysis. 95% c.i.: 95% confidence interval; 2SD: two standard deviation corrected by the Student's *t* factor. Net isotope fractionation $\Delta^7Li_{l\text{-}s}$ and $\Delta^{41}K_{l\text{-}s}$ during dissolution reported in this paper could be calculated by the difference between dissolved isotopic composition (shown in this table) and initial rock isotopic composition. n.d.: not determined. Temp.: temperature.

−0.07‰ after ~4 wt% K for granite and ~ 11 wt% K for basalt leached from the silicate skeleton with 5 mM CA, and reached −0.06‰ after ~14 wt% K for basalt leached using 5 mM OA at 25 °C. The evolution patterns of liquid $\delta^{41}K$ in the two acid systems are indistinguishable.

5. Discussion

5.1. Dissolution and fractionation patterns

Both proton-driven and ligand-driven dissolution of basalt and granite display substantial variations in solute isotopic compositions of Li and K in time-series (Figs. 6–7). The Li and K isotope fractionation between fluids and initial silicates display an undulating trend with an initial increase, followed by a decrease to about zero. There is no apparent difference in the isotope fractionation degree at the initial dissolution stage during proton-driven and ligand-driven dissolution. This reveals the negligible role of the ligand-cation complexation of Li^+ and K^+ and associated isotope behavior in comparison to multivalent ions of high ionic potential (as Fe^{3+}, Morgan et al., 2010). In contrast, Fe isotope fractionation in the presence of organic ligands, is different from that of mineral acids (Wiederhold et al., 2006; Chapman et al., 2009; Kiczka et al., 2010a). The main reason for this is the high affinity of Fe to organic ligands and the excess of dissolved Fe related to Li^+ and K^+. A similar argument has been made for Zn (Weiss et al., 2014). We distinguish three phases of ion release in the dissolution profiles of Li and K (Figs. 4–7): (i) an incipient period of rapid release with significantly low initial pH and the liberation of light isotopes into fluids (only over days), followed by (ii) slower, long term dissolution with decreasing isotope fractionation, and/or end up with resorption of isotopically light isotopes to solids. This isotopic variation reflects an interplay of several fractionation processes. In principle, three compatible mechanisms potentially affect the degree of Li and K isotope fractionation during silicate dissolution: (i) incongruent dissolution of various silicate phases, in which overall isotopic effects rely on the

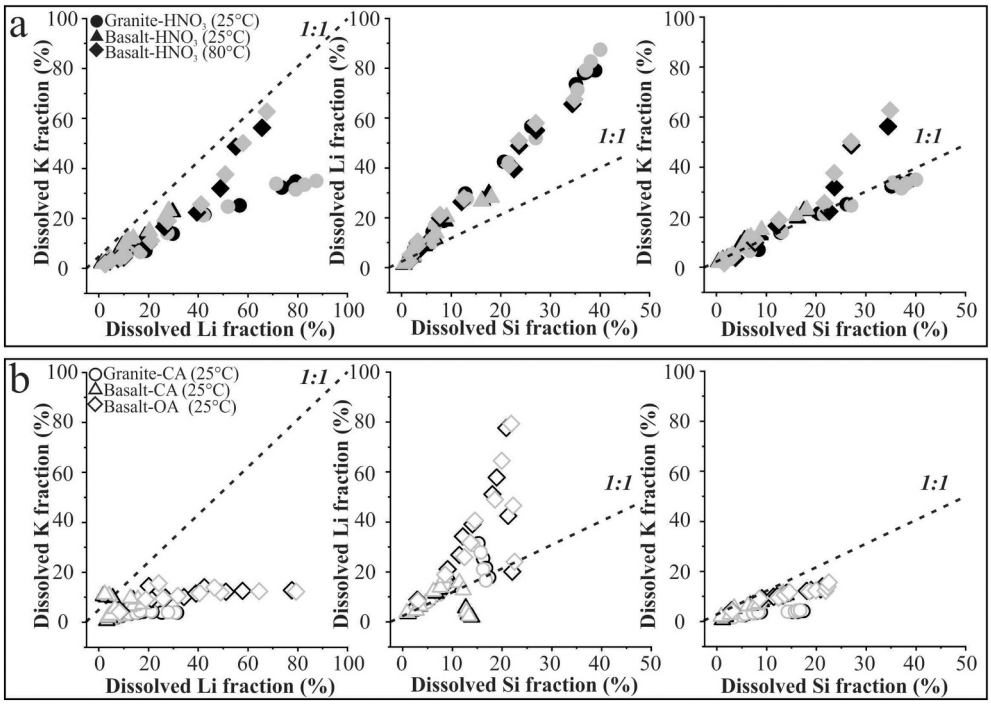

Fig. 5. Stoichiometric characterization of the silicate dissolution during proton-driven (solid symbols) and ligand-driven (hollow symbols) dissolution. In the proton-driven experiments, the features of (a) Li to K, Si to Li and Si to K are shown. In the ligand-driven experiments, the features of (b) Li to K, Si to Li and Si to K are shown. Dashed lines of idealized element fraction ratio in the total element pool in silicates (1:1) are exhibited and can be compared for stoichiometry. All experiments were conducted in duplicate (black: $EXP_{(1)}$; grey: $EXP_{(2)}$).

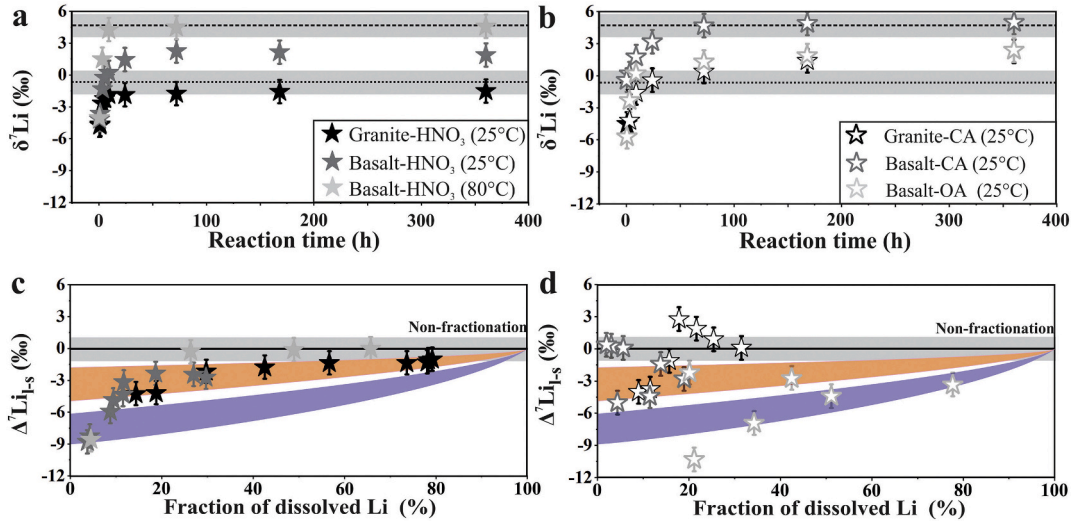

Fig. 6. The isotope fractionation of Li during silicate dissolution. Aqueous δ^7Li as a function of reaction time during (a) proton-driven and (b) ligand-driven dissolution. The dashed and dotted lines represent the Li isotopic compositions of BHVO-2 (4.6‰) and GSP-2 (0.6‰), respectively. The error bar (grey area) is the long-term analytical uncertainty (2SD = 1.1‰). Net isotope fractionations between liquids (l) and solids (s) $\Delta^7Li_{l\text{-}s}$ as a function of dissolved Li during (c) proton-driven and (d) ligand-driven dissolution. The orange and purple regions show curve-fit data of the mass-dependent Li^+ diffusion in liquid water (Bourg et al., 2010, $\beta = 0.0171 \pm 0.0159$) and surface ion desolvation (Hofmann et al., 2012, $\alpha = 0.9925 \pm 0.0014$). (For interpretation of the references to colour in this figure legend, the reader is referred to the web version of this article.)

isotopic compositions and dissociation kinetics of each silicate phases (ii) backwards reaction involving uptake of pre-released cations, which probably balance or retard the dissolution and (iii) the competition between kinetic and equilibrium fractionation including multi-steps with different isotopic effects. Herein, each of above possibilities is discussed.

5.2. Differential dissolution of minerals

Silicate dissolution involves simultaneous dissociation of a mixed assemblage of minerals of varying solubilities and isotopic compositions. One way to circumvent the experimental problems related to studied polyminerallic systems is the ideal of free isotope mixing of two or more pools with distinct isotopic signals in silicate rocks. One piece of evidence in support of this hypothesis is recent theoretical calculations performed (Li et al., 2017; Li et al., 2019c; Zeng et al., 2019) that shows isotope fractionations between surrounding water medium and precipitated minerals ($\Delta^{41}K_{solu\text{-}miner}$) are largely variable (from negative to positive) and dependent on mineralogy. Additional evidence can be derived from experimental and filed observation of magmatic diffusion, which can cause large Li isotope fractionation between rock-forming minerals (e.g., Richter et al., 2006,

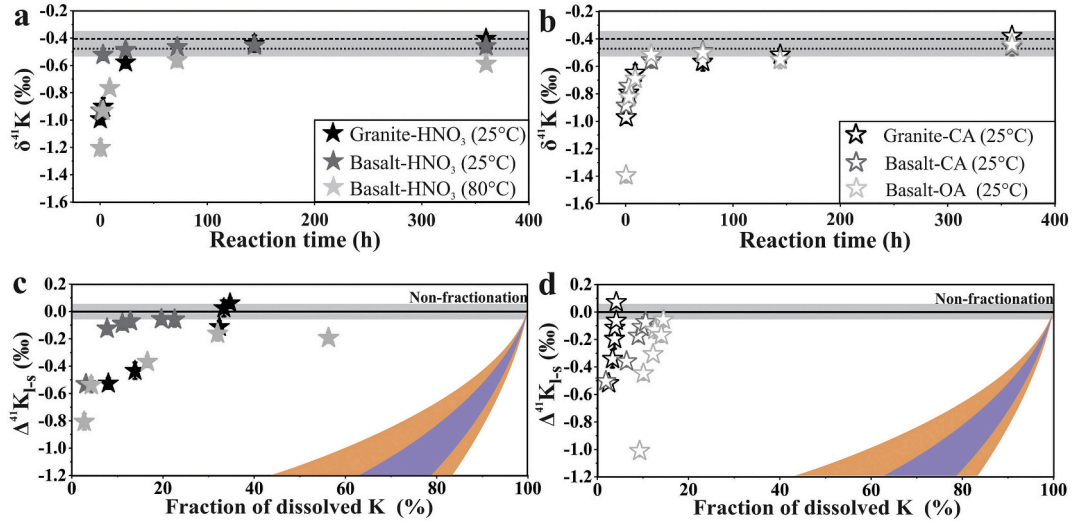

Fig. 7. The isotope fractionation of K during silicate dissolution. Aqueous $\delta^{41}K$ as a function of reaction time during (a) proton-driven and (b) ligand-driven dissolution. The dashed and dotted lines denote the K isotopic compositions of BHVO-2 (−0.40‰) and GSP-2 (−0.46‰), respectively. The error bar (grey area) displays the 95% confidence interval calculated from standard error of the mean corrected using the Student *t*-factor (95%c.i., see details in Hu et al., 2018). We note that the error bar is almost identical to the symbol size used in the plots. Net K isotope fractionations between liquids (l) and solids (s) $\Delta^{41}K_{l\text{-}s}$ as a function of dissolved K during (c) proton-driven and (d) ligand-driven dissolution. Orange and purple regions show the curve-fit result of mass-dependent diffusion of K^+ in water (Bourg et al., 2010, $\beta = 0.049 \pm 0.017$) and surface desolvation (Hofmann et al., 2012, $\alpha = 0.9976 \pm 0.0004$). (For interpretation of the references to colour in this figure legend, the reader is referred to the web version of this article.)

2014; Wunder et al., 2007; Li et al., 2018).

Nevertheless, differential rock dissolution is unlikely a primary factor of observed isotope fractionation. A major reason is that time-series Li and K isotope patterns are nearly identical, independent of lithology (basalt vs. granite) and the preferential dissolution of micaceous or feldspar minerals based on XRD. In addition, a lack of the correlation between $\delta^{41}K_{bulk}$ and K_2O in lavas at Northeast China opposes the argument of fractionation of K-bearing minerals in controlling isotopic difference in lavas (Sun et al., 2020). As lines of supportive evidence, K—Li isotope fractionation during magmatic differentiation is minor (Tomascak et al., 1999; Tuller-Ross et al., 2019). Both experiment and field studies have implied rock dissolution without Li isotope fractionations (Pistiner and Henderson, 2003; Lemarchand et al., 2010). We infer that differential dissolution is not a primary control in the experiments.

5.3. Evaluation of backward reactions

Through fluid-rock interaction, backward reactions such as resorption and reprecipitation, potentially results in interferences with dissolution stoichiometry and the degree of isotope fractionation as the reaction continues. In closed batch sets, the gradual accumulation of ions in the solute and reduction in dissolution kinetics drive solutions to saturation, and isotope behavior may be scaled by the relative intensity between forward and backward reactions.

As for Li isotopes, positive shifts in solute isotopic composition from initial silicate sources imply the resorption of lighter Li isotopes during the late stage of ligand-driven dissolution. This feature is explained by two possible mechanisms. First, pre-released Li is isotopically lighter during the early dissolution stage and subsequent resorption could cause the Li left in solutions isotopically heavier. The resorption of Li is supported by decreases in solute Li concentration after 100 h (Fig. 3) and a sudden transition in Li/Si stoichiometry is a result of Li^+ resorption at the late dissolution stage (Fig. 4). Second, the resorption of lighter Li is facilitated by enhanced surface electrostatic attraction and subsequent complexation onto silicates (Pistiner and Henderson, 2003; Millot and Girard, 2007; Wimpenny et al., 2015; Li et al., 2020a, 2020b). Alternatively, surface reprecipitation potentially incorporates light Li isotopes in newly-formed phases (Vigier et al., 2008; Hindshaw et al., 2019; Pogge von Strandmann et al., 2019). For example, as the solute pH increases in excess of ~5, the spontaneous precipitation of isotopically heavy Fe becomes vital during the dissolution of phyllosilicates and goethite (Chapman et al., 2009; Wiederhold et al., 2006). However, Li sinks in secondary phases are less plausible according to XRD data. We note that such a reverse pattern in the Li isotopic behavior was not found during proton-driven dissolution due to the protonation of solid surface sites at low pH. In contrast, there is no observation of K resorption and associated isotope shifts in both acidic systems. We infer that surface complexation of K^+ is limited by the weaker hydration of K^+ (−320 kJ/mol) relative to Li^+ (−520 kJ/mol). Cation replacement by Fe^{3+} and Al^{3+} inhibits the direct bonding of K^+ to solids.

Reasons for the backward reaction of Li during ligand-driven dissolution can be envisaged. First, silicate residuals have a higher density of negative surface charges because of the deprotonation of silanol (≡Si–OH) sites at a higher pH ~ 4.5 of ligand-driven dissolution compared to a lower pH ~ 0.2 during proton-driven dissolution (e.g., Wetzel et al., 2014; Thanh and Sprik, 2016). Supportively, the point of zero charges (pH_{pzc}) of biotite, quartz, and feldspar, is in a range of 2–3 (Weiss et al., 2014); so these minerals may electrostatically retain or bond to released cations. A dominant dissolved Li phase is ionic Li $(H_2O)_4^+$ under acidic conditions, and cations are strongly electrostatically attracted with pH increasing. Second, forward dissolution to backreaction rate ratio is high in proton-driven dissolution, and backward reactions may not appear and interfere with the isotopic effects of the forward reactions. Since deprotonated silanol groups on silicates favor polymerization along with the adsorption of monovalent cations, forward dissolution of Si was retarded, which is the case in ligand-driven dissolution (Dultz et al., 2016). Moreover, the presence of organic acids affects the isotope exchange between solids and waters, which is common in nature.

5.4. Kinetic and equilibrium controls

To examine another hypothesis (kinetic vs. equilibrium), Li and K isotopic mass balances are required to interpret isotopic fluctuation. A simple method for a quantitative interpretation of Li and K isotopic

behavior is the application of the Rayleigh-type model (Fig. 6c–d and Fig. 7c–d). This model simply assumes Li and K isotopes are homogeneously distributed in rocks and then released from silicate structures in a rate-limiting step, which could be described by the follow equations. Although well mixed Li and K isotopes in the solids and homogeneous releases in the experiment are unlikely, we tentatively used the Rayleigh model to approximate isotope fractionation processes, given the limited isotope fractionation of Li and K during magmatic processes (Tomascak et al., 1999; Tuller-Ross et al., 2019).

$$\delta^{7}Li_{Liquid} = \left(\frac{\alpha \times \delta^{7}Li_{rock} + 1000f_{Li} \times (\alpha - 1)}{\alpha\,(1 - f_{Li}) + f_{Li}}\right); \delta^{41}K_{liquid} = \left(\frac{\alpha \times \delta^{41}K_{rock} + 1000f_{K} \times (\alpha - 1)}{\alpha\,(1 - f_{K}) + f_{K}}\right) \quad (6)$$

Where f denotes the percentage of Li or K released from rocks and the fractionation factor $\alpha = [(^{7}Li/^{6}Li)_{fluid}/(^{7}Li/^{6}Li)_{soli}$ or $[(^{41}K/^{39}K)_{fluid}/(^{41}K/^{39}K)_{solid}$. As for isotope interpretation, Li^{+} and K^{+} diffusion in liquid water ($\beta_{Li} = 0.0171 \pm 0.0159$; $\beta_{K} = 0.049 \pm 0.017$; Bourg et al., 2010) was modeled, which partially explained the initial kinetic isotope signal (i.e., light isotopes in fluids). However, one perplexing issue is that the initial Li isotope ratios in the solutions are even lower than the diffusion fits. The kinetic ion-desolvation theory reported in Hofmann et al. (2012) has been applied to explain isotope effects during interfacial precipitation. Because both ion-solvation and desolvation reactions in the non-equilibrium states follow the reaction-rate theory (Hänggi et al., 1990), we tentatively used reported parameters for curve fitting. Ion-solvation fractionation was modeled ($\alpha_{Li} = 0.9925 \pm 0.0014$; $\alpha_{K} = 0.9976 \pm 0.0004$), which explains the significant enrichment of light Li isotopes near the onset of the experiment.

The presence of the leached layer has been verified by XPS analysis and is a prerequisite for kinetic isotope effects during dissolution (Brantley et al., 2004). Since Si has a higher electronegativity value (1.9) than multivalent cations in silicates (Fe, 1.8; Mg, 1.3; Al, 1.6), electrons in mineral structures preferentially move towards Si atoms, rendering their lower binding energies (BE) and higher energy intensities. Hence, Si bonding energy measured by XPS shifts to higher energy ranges after the cation is released from the lattice. This reveals reduced valence electron density on the Si nuclei, along with the release of metal cations from basalt and granite during dissolution (Fig. 3a–3b). Silicate dissolution often involves a gel-like film, commonly known as “the leached layer of silicate structure”. The chemically and structurally distinct zone is expected to be formed and restructured, releasing silica units via different degrees of polymerization (Casey et al., 1993; Weissbart and Rimstidt, 2000), resulting in changes in BE. We thereby determined two major silicon species, i.e., SiO_x ($x > 2$) in the high BE range (~103–104 eV) and SiO_2 in the low BE range (~102–103 eV). Because of surface hydrolysis and condensation, silica-enriched leached layers were subsequently developed through gradual transformation of crystalline SiO_X to amorphous silica phases. Since SiO_X sites have been recognized to be chemically more reactive than SiO_2 sites (Iler, 1979), the formation of the leached layer made silicate surfaces less prone to elemental exchange with coexisting dissolved phases. Therefore, we adopted the ratio of SiO_2/SiO_x in reacted solids relative to pristine rocks as the criteria for determining leached layer formation (low SiO_x/SiO_2 ratios imply more developed leached layer). The development of the leached layer in both dissolution systems (25 °C) could be identified.

We note that solute K isotope patterns cannot be reasoned by the two kinetic paths, which are likely affected by sluggish K liberation supported by the dissolution stoichiometry (Fig. 5). During proton-driven dissolution, silicate-hosted Li was preferentially released relative to structural K in the lattice or interlayer space, and releasing tetrahedral Si was retarded. This feature is derived from data overlapping the line of 1:1 unit slope passing through an origin (Fig. 5a), implying higher proportions of Li than the release of K—Si. Only at 80 °C, K release was near stoichiometric to the liberation of Li. During ligand-driven dissolution, Li liberation was not stoichiometric to K—Si release, and K release was retarded at a higher level compared to the pattern of proton-driven dissolution (Fig. 5b). Retarded K release kinetics was reported by Kiczka et al. (2010a), with respect to Fe isotope fractionation in a similar dissolution system. This feature is reasoned by the incongruent dissolution of octahedral and tetrahedral units in K-bearing silicate minerals. As supportive evidence, congruent silicate dissolution could be endorsed by the dissolution stoichiometry (Fig. 5).

During the late-stage dissolution, the disappearance of Li and K isotope fractionation can be reasoned by (i) masking effects from intensive dissolution without isotope fractionation, (ii) subsequent destruction of $^{7}Li/^{41}K$-enriched leached layers, and/or (iii) the equilibrium fractionation depending on structural coordination change between solids and liquids. The first mechanism has been reported in Wiederhold et al. (2006), who stated that If the cation release is accompanied by its coordinating oxygen atoms within the silicate structures, i.e., Li/K-O bonding is complete, no isotopic fractionation should appear. The second mechanism is induced by enrichment of heavy isotopes in the leached layer by incipient kinetic effects, and lateral dissociation of the leached layer. Theoretical and spectroscopic data confirm that ionic K^{+} has a lower coordination number (~6) and shorter K—O bonding length ($(2.7–2.8) \cdot 10^{2}$ pm) than those of K^{+} in silicate structures ($N \sim 6–9$, $(2.7–3.2) \cdot 10^{2}$ pm) (Kamijo et al., 1996; Cibin et al., 2005; Glezakou et al., 2006; Liu et al., 2010). The third mechanism enables partitioning of isotopically heavier K into solutions due to the coordination change, compensating for initial kinetic effects. Likewise, dissolved Li^{+} has a lower coordination number (~4) and a shorter Li—O bond length (~1.9 Å) than Li in silicate lattices ($N \sim 6$, ~1.9–2.3 Å) (Hannon et al., 1992; Yamaguchi et al., 2010; Liu et al., 2018). Therefore, kinetic and equilibrium reactions during successive dissolution steps control fluid isotope signals.

6. Summary and implications

We experimentally investigated Li and K isotope fractionation during closed, batch silicate dissolution. A combination of stoichiometry, spectroscopic analysis, and isotope analysis in proton-driven and ligand-driven dissolution experiments offer insights into Li and K isotopic behavior. The results do not fully conform to our hypothesis (i.e., Li and K isotopes behave similarly in both systems). The two experiment systems show distinct solute chemical features (i.e., ligand type and pH) over the course of this study (15 days), yet the fundamental isotopic responses of Li and K released into fluids are initially the same (kinetic isotope fractionation caused by ionic diffusion and/or solvation). Nevertheless, the isotope fractionation of Li is reversed during the late stage of dissolution, whereas the fractionation of K reached both chemical and isotope equilibrium subsequently. The behaviors of Li and K during ligand-driven and proton-driven dissolution are not the same, and the difference is reasoned by ligand-cation interactions and backward-reactions. Previous investigations under similar experimental conditions have shown that this is also the case for other metal isotopes (e.g., Fe and Zn) (Wiederhold et al., 2006; Chapman et al., 2009; Kiczka et al., 2010a; Weiss et al., 2014). In summary, the exchange of metals and isotopes during dissolution likely occurs in multiple steps: (i) kinetic loss of ions from silicate minerals in rocks into fluids, (ii) the break-down of primary silicates and (iii) back-reactions (adsorption and/or precipitation). The first step promotes the liberation of light isotopes, which then can be balanced by the second step (or affected by ligand- cation interaction). The third step may occur, producing different isotope behaviors.

The results of this study have significant implications for the interpretation of isotopic signatures in natural weathering systems. First, the preservation of kinetic isotope imprints should be the case in natural environments, despite its transit feature in this study. The kinetic isotope signals may be recorded in incomplete or unidirectional reactions with substantial undersaturation. Based on the observation of our work, the

kinetic Li and K isotope signals could be overprinted within one day. We note that these experiments were performed in batch systems rather than reactors in flow-through mode. The dissolution of silicate minerals in both basalt and granite is controlled by pH, concentrations of organic ligand, and activities of some major cations such as Fe^{3+} and Al^{3+}. The concentration of multivalent cations gradually increases as dissolution progresses, and affects the overall reaction rate since the saturation state of minerals changes during reactions. Therefore, the time period that fluids are at far-from-chemical equilibrium conditions may be extended. Given that, natural kinetic isotope imprints during dissolution might be preserved in some cases, such as persistent strong disequilibria in soil porewater. Or, reacted solutions can be instantaneously isolated from reacted solids in weathering and hydrothermal settings where the reaction process is rapid under continuous fluxes. As for the former, the diffusion of Li has been documented in the saprolites formed on a diabase dike at South Carolina (Teng et al., 2010). As for the latter, the high δ^7Li values in altered ocean crust (on-axis) are most readily ascribed to diffusive fractionation of isotopes during leaching from plagioclase (Brant et al., 2012). In addition, the outcome suggests that the isotope behaviors of Li and K are independent of kinetics, stoichiometry, or lithology during dissolution, which can be affected by temperature (25–80 °C) and organic ligands. Long-term back-reaction and the corresponding isotope effect cannot be ignored in the presence of organic ligands and/or increases in solute pH for Li^+, as well as Mg^{2+}, Fe^{3+} and Al^{3+} during silicate dissolution (e.g., Brantley et al., 2004; Wiederhold et al., 2006; Ryu et al., 2011). Critically, the resorption of Li^+ could result in significant isotope effects. It is reasonable to infer that surface K may be structurally replaced by coexisting cations. If so, clay incorporation rather than adsorption is a major control on K isotope fractionation in weathering. Systematic clay adsorption experiments are needed to test this hypothesis. In comparison, Li isotope fractionation could be induced by adsorption and incorporation with different fractionation magnitudes (e.g., Vigier et al., 2008; Wimpenny et al., 2015; Hindshaw et al., 2019; Li and Liu, 2020b). The relative contributions of the two competing mechanisms in controlling Li isotopic fractionation are difficult to determine, complicating the interpretation of geological Li records. Hence, we consider K isotopes to be more promising as an isotope tool for weathering reconstruction as K isotopes have been fractionated by weathering with less interference compared to Li isotopes in nature.

Supplementary data to this article can be found online at https://doi.org/10.1016/j.chemgeo.2021.120142.

Declaration of Competing Interest

None.

Acknowledgements

We acknowledge funding support from the NSF Career Award (EAR-1848153) and DOD Army Research Office Grant (W911NF-17-2-0028) to X.-M. Liu, and the Martin fellowship from the University of North Carolina to W. Li. K. Wang and P. Koefoed thank the McDonnell Center for the Space Sciences for financial support. We thank Editor Dr. Donald Porcelli, Dr. Paul Tomascak, and two anonymous reviewers whose comments helped us improve the manuscript. We also wish to thank for XPS analysis at the Chapel Hill Analytical and Nanofabrication Laboratory, CHANL, the member of North Carolina Research Triangle Nanotechnology Network. UNC CHANL is supported by the National Science Foundation (No. ECCS-1542015), as a part of National Nanotechnology Coordinated Infrastructure.

References

Amiotte Suchet, P., Probst, J.-L., Ludwig, W., 2003. Worldwide distribution of continental rock lithology: Implications for the atmospheric/soil CO_2 uptake by continental weathering and alkalinity river transport to the oceans. Glob. Biogeochem. Cycles 17 (n/a-n/a). https://doi.org/10.1029/2002gb001891.

Balland-Bolou-Bi, C., Bolou-Bi, E.B., Vigier, N., Mustin, C., Poszwa, A., 2019. Increased Mg release rates and related Mg isotopic signatures during bacteria-phlogopite interactions. Chem. Geol. 506, 17–28. https://doi.org/10.1016/j.chemgeo.2018.12.020.

Bataille, C.P., Willis, A., Yang, X., Liu, X.M., 2017. Continental igneous rock composition: a major control of past global chemical weathering. Sci. Adv. 3 https://doi.org/10.1126/sciadv.1602183.

Bayon, G., Burton, K.W., Soulet, G., Vigier, N., Dennielou, B., Etoubleau, J., Ponzevera, E., German, C.R., Nesbitt, R.W., 2009. Hf and Nd isotopes in marine sediments: Constraints on global silicate weathering. Earth Planet. Sci. Lett. 277, 318–326. https://doi.org/10.1016/j.epsl.2008.10.028.

Bourg, I.C., Richter, F.M., Christensen, J.N., Sposito, G., 2010. Isotopic mass dependence of metal cation diffusion coefficients in liquid water. Geochim. Cosmochim. Acta 74, 2249–2256. https://doi.org/10.1016/j.gca.2010.01.024.

Brant, C., Coogan, L.A., Gillis, K.M., Seyfried, W.E., Pester, N.J., Spence, J., 2012. Lithium and Li-isotopes in young altered upper oceanic crust from the East Pacific rise. Geochim. Cosmochim. Acta 96, 272–293. https://doi.org/10.1016/j.gca.2012.08.025.

Brantley, S.L., Liermann, L.J., Guynn, R.L., Anbar, A., Icopini, G.A., Barling, J., 2004. Fe isotopic fractionation during mineral dissolution with and without bacteria. Geochim. Cosmochim. Acta 68, 3189–3204. https://doi.org/10.1016/j.gca.2004.01.023.

Casey, W.H., Westrich, H.R., Banfield, J.F., Ferruzzi, G., Arnold, G.W., 1993. Leaching and reconstruction at the surfaces of dissolving chain-silicate minerals. Nature 366, 253–256. https://doi.org/10.1038/366253a0.

Chapman, J.B., Weiss, D.J., Shan, Y., Lemburger, M., 2009. Iron isotope fractionation during leaching of granite and basalt by hydrochloric and oxalic acids. Geochim. Cosmochim. Acta 73, 1312–1324. https://doi.org/10.1016/j.gca.2008.11.037.

Chen, H., Tian, Z., Tuller-Ross, B., Korotev, R.L., Wang, K., 2019. High-precision potassium isotopic analysis by MC-ICP-MS: an inter-laboratory comparison and refined K atomic weight. J. Anal. At. Spectrom. 34, 160–171. https://doi.org/10.1039/c8ja00303c.

Chen, H., Liu, X.M., Wang, K., 2020. Potassium isotope fractionation during chemical weathering of basalts. Earth Planet. Sci. Lett. 539 https://doi.org/10.1016/j.epsl.2020.116192.

Cibin, G., Mottana, A., Marcelli, A., Brigatti, M.F., 2005. Potassium coordination in trioctahedral micas investigated by K-edge XANES spectroscopy. Mineral. Petrol. 85, 67–87. https://doi.org/10.1007/s00710-005-0099-z.

Cotta, A.J.B., Enzweiler, J., Wilson, S.A., Pérez, C.A., Nardy, A.J.R., Larizzatti, J.H., 2007. Homogeneity of the geochemical reference material BRP-1 (paranábasin basalt) and assessment of minimum mass. In: Geostandards and Geoanalytical Research, pp. 379–393. https://doi.org/10.1111/j.1751-908X.2007.00111.x.

De La Rocha, C.L., DePaolo, D.J., 2000. Isotopic evidence for variations in the marine calcium cycle over the cenozoic. Science (80-.) 289, 1176–1178. https://doi.org/10.1126/science.289.5482.1176.

Dellinger, M., Gaillardet, J., Bouchez, J., Calmels, D., Louvat, P., Dosseto, A., Gorge, C., Alanoca, L., Maurice, L., 2015. Riverine Li isotope fractionation in the Amazon River basin controlled by the weathering regimes. Geochim. Cosmochim. Acta 164, 71–93. https://doi.org/10.1016/j.gca.2015.04.042.

Dultz, S., Behrens, H., Helsch, G., Deubener, J., 2016. Electrolyte effects on surface chemistry of basaltic glass in the initial stages of dissolution. Chem. Geol. 426, 71–84. https://doi.org/10.1016/j.chemgeo.2016.01.027.

Edmond, J.M., 1992. Himalayan tectonics, weathering processes, and the strontium isotope record in marine limestones. Science (80-.) 258, 1594–1597. https://doi.org/10.1126/science.258.5088.1594.

Eiriksdottir, E.S., Gislason, S.R., Oelkers, E.H., 2015. Direct evidence of the feedback between climate and nutrient, major, and trace element transport to the oceans. Geochim. Cosmochim. Acta 166, 249–266. https://doi.org/10.1016/j.gca.2015.06.005.

Fernandez, A., Borrok, D.M., 2009. Fractionation of Cu, Fe, and Zn isotopes during the oxidative weathering of sulfide-rich rocks. Chem. Geol. 264, 1–12. https://doi.org/10.1016/j.chemgeo.2009.01.024.

Gaillardet, J., Dupré, B., Louvat, P., Allègre, C.J., 1999. Global silicate weathering and CO2 consumption rates deduced from the chemistry of large rivers. Chem. Geol. 159, 3–30. https://doi.org/10.1016/S0009-2541(99)00031-5.

Glezakou, V.A., Chen, Y., Fulton, J.L., Schenter, G.K., Dang, L.X., 2006. Electronic structure, statistical mechanical simulations, and EXAFS spectroscopy of aqueous potassium. Theor. Chem. Accounts 115, 86–99. https://doi.org/10.1007/s00214-005-0054-4.

Goldich, S.S., 1938. A Study in Rock-Weathering. J. Geol. 46, 17–58. https://doi.org/10.1086/624619.

Hänggi, P., Talkner, P., Borkovec, M., 1990. Reaction-rate theory: Fifty years after Kramers. Rev. Mod. Phys. 62, 251–341. https://doi.org/10.1103/RevModPhys.62.251.

Hannon, A.C., Vessal, B., Parker, J.M., 1992. The structure of alkali silicate glasses. J. Non-Cryst. Solids 150, 97–102. https://doi.org/10.1016/0022-3093(92)90102-P.

Hartmann, J., West, A.J., Renforth, P., Köhler, P., De La Rocha, C.L., Wolf-Gladrow, D.A., Dürr, H.H., Scheffran, J., 2013. Enhanced chemical weathering as a geoengineering strategy to reduce atmospheric carbon dioxide, supply nutrients, and mitigate ocean acidification. Rev. Geophys. 51, 113–149. https://doi.org/10.1002/rog.20004.

Hausrath, E.M., Navarre-Sitchler, A.K., Sak, P.B., Williams, J.Z., Brantley, S.L., 2011. Soil profiles as indicators of mineral weathering rates and organic interactions for a Pennsylvania diabase. Chem. Geol. 290, 89–100. https://doi.org/10.1016/j.chemgeo.2011.08.014.

Henchiri, S., Gaillardet, J., Dellinger, M., Bouchez, J., Spencer, R.G.M., 2016. Riverine dissolved lithium isotopic signatures in low-relief Central Africa and their link to weathering regimes. Geophys. Res. Lett. 43, 4391–4399. https://doi.org/10.1002/2016GL067711.

Henderson, G.M., 2002. New oceanic proxies for paleoclimate. Earth Planet. Sci. Lett. 203, 1–13. https://doi.org/10.1016/S0012-821X(02)00809-9.

Hindshaw, R.S., Tosca, R., Goût, T.L., Farnan, I., Tosca, N.J., Tipper, E.T., 2019. Experimental constraints on Li isotope fractionation during clay formation. Geochim. Cosmochim. Acta 250, 219–237. https://doi.org/10.1016/j.gca.2019.02.015.

Hofmann, A.E., Bourg, I.C., DePaolo, D.J., 2012. Ion desolvation as a mechanism for kinetic isotope fractionation in aqueous systems. Proc. Natl. Acad. Sci. U. S. A. 109, 18689–18694. https://doi.org/10.1073/pnas.1208184109.

Holland, H.D., 2005. Sea level, sediments and the composition of seawater. Am. J. Sci. 305, 220–239. https://doi.org/10.2475/ajs.305.3.220.

Hu, Y., Chen, X.Y., Xu, Y.K., Teng, F.Z., 2018. High-precision analysis of potassium isotopes by HR-MC-ICPMS. Chem. Geol. 493, 100–108. https://doi.org/10.1016/j.chemgeo.2018.05.033.

Huang, K.F., You, C.F., Liu, Y.H., Wang, R.M., Lin, P.Y., Chung, C.H., 2010. Low-memory, small sample size, accurate and high-precision determinations of lithium isotopic ratios in natural materials by MC-ICP-MS. J. Anal. At. Spectrom. 25, 1019–1024. https://doi.org/10.1039/b926327f.

Huh, Y., Chan, L.H., Zhang, L., Edmond, J.M., 1998. Lithium and its isotopes in major world rivers: implications for weathering and the oceanic budget. Geochim. Cosmochim. Acta 62, 2039–2051. https://doi.org/10.1016/S0016-7037(98)00126-4.

Huh, Y., Chan, L.H., Edmond, J.M., 2001. Lithium isotopes as a probe of weathering processes: Orinoco River. Earth Planet. Sci. Lett. 194, 189–199. https://doi.org/10.1016/S0012-821X(01)00523-4.

Iler, R.K., 1979. The Chemistry of Silica. https://doi.org/10.1016/0160-9327(80)90074-5.

Jochum, K.P., Weis, U., Schwager, B., Stoll, B., Wilson, S.A., Haug, G.H., Andreae, M.O., Enzweiler, J., 2016. Reference values following ISO guidelines for frequently requested rock reference materials. Geostand. Geoanal. Res. 40, 333–350. https://doi.org/10.1111/j.1751-908X.2015.00392.x.

Kamijo, N., Handa, K., Umesaki, N., 1996. Soft x-ray xafs studies on the local structure of k2o-sio2 glasses. Mater. Trans. JIM 37, 927–931. https://doi.org/10.2320/matertrans1989.37.927.

Kiczka, M., Wiederhold, J.G., Frommer, J., Kraemer, S.M., Bourdon, B., Kretzschmar, R., 2010a. Iron isotope fractionation during proton- and ligand-promoted dissolution of primary phyllosilicates. Geochim. Cosmochim. Acta 74, 3112–3128. https://doi.org/10.1016/j.gca.2010.02.018.

Kiczka, M., Wiederhold, J.G., Kraemer, S.M., Bourdon, B., Kretzschmar, R., 2010b. Iron isotope fractionation during Fe uptake and translocation in alpine plants. Environ. Sci. Technol. 44, 6144–6150. https://doi.org/10.1021/es100863b.

Kimball, B.E., Rimstidt, J.D., Brantley, S.L., 2010. Chalcopyrite dissolution rate laws. Appl. Geochem. 25, 972–983. https://doi.org/10.1016/j.apgeochem.2010.03.010.

Kisakurek, B., James, R.H., Harris, N.B.W., 2005. Li and δ^7Li in Himalayan rivers: Proxies for silicate weathering? Earth Planet. Sci. Lett. 237, 387–401. https://doi.org/10.1016/j.epsl.2005.07.019.

Korotev, R.L., 1996. A self-consistent compilation of elemental concentration data for 93 geochemical reference samples. Geostand. Newslett. 20, 217–245. https://doi.org/10.1111/j.1751-908X.1996.tb00185.x.

Lemarchand, E., Chabaux, F., Vigier, N., Millot, R., Pierret, M.C., 2010. Lithium isotope systematics in a forested granitic catchment (Strengbach, Vosges Mountains, France). Geochim. Cosmochim. Acta 74, 4612–4628. https://doi.org/10.1016/j.gca.2010.04.057.

Li, W., Liu, X.M., 2020a. Mobilization and partitioning of rare earth elements in the presence of humic acids and siderophores. Chemosphere 126801. https://doi.org/10.1016/j.chemosphere.2020.126801.

Li, W., Liu, X.M., 2020b. Experimental investigation of lithium isotope fractionation during kaolinite adsorption: Implications for chemical weathering. Geochim. Cosmochim. Acta 284, 156–172. https://doi.org/10.1016/j.gca.2020.06.025.

Li, W., Beard, B.L., Li, S., 2016. Precise measurement of stable potassium isotope ratios using a single focusing collision cell multi-collector ICP-MS. J. Anal. At. Spectrom. 31, 1023–1029. https://doi.org/10.1039/c5ja00487j.

Li, W., Kwon, K.D., Li, S., Beard, B.L., 2017. Potassium isotope fractionation between K-salts and saturated aqueous solutions at room temperature: Laboratory experiments and theoretical calculations. Geochim. Cosmochim. Acta 214, 1–13. https://doi.org/10.1016/j.gca.2017.07.037.

Li, J., Huang, X.L., Wei, G.J., Liu, Y., Ma, J.L., Han, L., He, P.L., 2018. Lithium isotope fractionation during magmatic differentiation and hydrothermal processes in rare-metal granites. Geochim. Cosmochim. Acta 240, 64–79. https://doi.org/10.1016/j.gca.2018.08.021.

Li, S., Li, W., Beard, B.L., Raymo, M.E., Wang, X., Chen, Y., Chen, J., 2019a. K isotopes as a tracer for continental weathering and geological K cycling. Proc. Natl. Acad. Sci. U. S. A. 116, 8740–8745. https://doi.org/10.1073/pnas.1811282116.

Li, W., Liu, X.M., Godfrey, L.V., 2019b. Optimisation of lithium chromatography for isotopic analysis in geological reference materials by MC-ICP-MS. Geostand. Geoanal. Res. 43, 261–276. https://doi.org/10.1111/ggr.12254.

Li, Y., Wang, W., Huang, S., Wang, K., Wu, Z., 2019c. First-principles investigation of the concentration effect on equilibrium fractionation of K isotopes in feldspars. Geochim. Cosmochim. Acta 245, 374–384. https://doi.org/10.1016/j.gca.2018.11.006.

Li, X., Han, G., Zhang, Q., Miao, Z., 2020a. Optimal separation method for high-precision K isotope analysis by using MC-ICP-MS with a dummy bucket. J. Anal. At. Spectrom. https://doi.org/10.1039/d0ja00127a.

Li, W., Liu, X.M., Chadwick, O.A., 2020b. Lithium isotope behavior in Hawaiian regoliths: Soil-atmosphere-biosphere exchanges. Geochim. Cosmochim. Acta 285, 175–192. https://doi.org/10.1016/j.gca.2020.07.012.

Lin, J., Liu, Y., Hu, Z., Yang, L., Chen, K., Chen, H., Zong, K., Gao, S., 2016. Accurate determination of lithium isotope ratios by MC-ICP-MS without strict matrix-matching by using a novel washing method. J. Anal. At. Spectrom. 31, 390–397. https://doi.org/10.1039/c5ja00231a.

Liu, X.M., Li, W., 2019. Optimization of lithium isotope analysis in geological materials by quadrupole ICP-MS. J. Anal. At. Spectrom. 34, 1708–1717. https://doi.org/10.1039/c9ja00175a.

Liu, X.M., Rudnick, R.L., 2011. Constraints on continental crustal mass loss via chemical weathering using lithium and its isotopes. Proc. Natl. Acad. Sci. U. S. A. 108, 20873–20880. https://doi.org/10.1073/pnas.1115671108.

Liu, Y., Lu, H., Wu, Y., Hu, T., Li, Q., 2010. Hydration and coordination of K+ solvation in water from ab initio molecular-dynamics simulation. J. Chem. Phys. 132 https://doi.org/10.1063/1.3369624.

Liu, S., Li, Y., Liu, Jie, Ju, Y., Liu, Jianming, Yang, Z., Shi, Y., 2018. Equilibrium lithium isotope fractionation in Li-bearing minerals. Geochim. Cosmochim. Acta 235, 360–375. https://doi.org/10.1016/j.gca.2018.05.029.

Ma, T., Weynell, M., Li, S.L., Liu, Y., Chetelat, B., Zhong, J., Xu, S., Liu, C.Q., 2020. Lithium isotope compositions of the Yangtze River headwaters: Weathering in high-relief catchments. Geochim. Cosmochim. Acta 280, 46–65. https://doi.org/10.1016/j.gca.2020.03.029.

Mavromatis, V., van Zuilen, K., Purgstaller, B., Baldermann, A., Nägler, T.F., Dietzel, M., 2016. Barium isotope fractionation during witherite (BaCO3) dissolution, precipitation and at equilibrium. Geochim. Cosmochim. Acta 190, 72–84. https://doi.org/10.1016/j.gca.2016.06.024.

Mavromatis, V., Harrison, A.L., Eisenhauer, A., Dietzel, M., 2017. Strontium isotope fractionation during strontianite (SrCO3) dissolution, precipitation and at equilibrium. Geochim. Cosmochim. Acta 218, 201–214. https://doi.org/10.1016/j.gca.2017.08.039.

Millot, R., Girard, J.P., 2007. Lithium isotope fractionation during adsorption onto mineral surfaces. In: Clays Nat. Eng. Barriers Radioact. Waste Confin. 3rd Int. Meet, pp. 307–308.

Millot, R., Vigier, N., Gaillardet, J., 2010. Behaviour of lithium and its isotopes during weathering in the Mackenzie Basin, Canada. Geochim. Cosmochim. Acta 74, 3897–3912. https://doi.org/10.1016/j.gca.2010.04.025.

Misra, S., Froelich, P.N., 2012. Lithium isotope history of cenozoic seawater: changes in silicate weathering and reverse weathering. Science (80-.) 335, 818–823. https://doi.org/10.1126/science.1214697.

Morgan, J.L., Wasylenki, L.E., Nuester, J., Anbar, A.D., 2010. Fe isotope fractionation during equilibration of Fe− organic complexes. Environ. Sci. Technol. 44 (16), 6095–6101. https://doi.org/10.1021/es100906z.

Morgan, L.E., Santiago Ramos, D.P., Davidheiser-Kroll, B., Faithfull, J., Lloyd, N.S., Ellam, R.M., Higgins, J.A., 2018. High-precision ^{41}K/^{39}K measurements by MC-ICP-MS indicate terrestrial variability of δ^{41}K. J. Anal. At. Spectrom. 33, 175–186. https://doi.org/10.1039/c7ja00257b.

Murphy, M.J., Porcelli, D., Pogge von Strandmann, P.A.E., Hirst, C.A., Kutscher, L., Katchinoff, J.A., Mörth, C.M., Maximov, T., Andersson, P.S., 2019. Tracing silicate weathering processes in the permafrost-dominated Lena River watershed using lithium isotopes. Geochim. Cosmochim. Acta 245, 154–171. https://doi.org/10.1016/j.gca.2018.10.024.

Olasolo, P., Juárez, M.C., Morales, M.P., Damico, S., Liarte, I.A., 2016. Enhanced geothermal systems (EGS): a review. Renew. Sust. Energ. Rev. https://doi.org/10.1016/j.rser.2015.11.031.

Pearce, C.R., Saldi, G.D., Schott, J., Oelkers, E.H., 2012. Isotopic fractionation during congruent dissolution, precipitation and at equilibrium: evidence from Mg isotopes. Geochim. Cosmochim. Acta 92, 170–183. https://doi.org/10.1016/j.gca.2012.05.045.

Pistiner, J.S., Henderson, G.M., 2003. Lithium-isotope fractionation during continental weathering processes. Earth Planet. Sci. Lett. 214, 327–339. https://doi.org/10.1016/S0012-821X(03)00348-0.

Pogge von Strandmann, P.A.E., Henderson, G.M., 2015. The Li isotope response to mountain uplift. Geology 43, 67–70. https://doi.org/10.1130/G36162.1.

Pogge von Strandmann, P.A.E., Fraser, W.T., Hammond, S.J., Tarbuck, G., Wood, I.G., Oelkers, E.H., Murphy, M.J., 2019. Experimental determination of Li isotope behaviour during basalt weathering. Chem. Geol. 517, 34–43. https://doi.org/10.1016/j.chemgeo.2019.04.020.

Richter, F.M., Mendybaev, R.A., Christensen, J.N., Hutcheon, I.D., Williams, R.W., Sturchio, N.C., Beloso, A.D., 2006. Kinetic isotopic fractionation during diffusion of ionic species in water. Geochim. Cosmochim. Acta 70, 277–289. https://doi.org/10.1016/j.gca.2005.09.016.

Richter, F.M., Bruce Watson, E., Chaussidon, M., Mendybaev, R., Christensen, J.N., Qiu, L., 2014. Isotope fractionation of Li and K in silicate liquids by Soret diffusion. Geochim. Cosmochim. Acta 138, 136–145. https://doi.org/10.1016/j.gca.2014.04.012.

Ryu, J.S., Jacobson, A.D., Holmden, C., Lundstrom, C., Zhang, Z., 2011. The major ion, δ44/40Ca, δ44/42Ca, and δ26/24Mg geochemistry of granite weathering at pH=1 and T=25°C: Power-law processes and the relative reactivity of minerals. Geochim. Cosmochim. Acta 75, 6004–6026. https://doi.org/10.1016/j.gca.2011.07.025.

Schauble, E.A., 2004. Applying stable isotope fractionation theory to new systems. Rev. Mineral. Geochem. https://doi.org/10.2138/gsrmg.55.1.65.

Stallard, R., 1995. Tectonic, Environmental, and Human Aspects of Weathering and Erosion: a Global Review from a Steady-State Perspective. Annu. Rev. Earth Planet. Sci. 23, 11–39. https://doi.org/10.1146/annurev.earth.23.1.11.

Sun, Y., Teng, F.Z., Hu, Y., Chen, X.Y., Pang, K.N., 2020. Tracing subducted oceanic slabs in the mantle by using potassium isotopes. Geochim. Cosmochim. Acta 278, 353–360. https://doi.org/10.1016/j.gca.2019.05.013.

Sutherland, D.G.J., Bancroft, G.M., Tan, K.H., 1992. Vibrational splitting in Si 2p core-level photoelectron spectra of silicon molecules. J. Chem. Phys. 97, 7918–7931. https://doi.org/10.1063/1.463467.

Teng, F.Z., Li, W.Y., Rudnick, R.L., Gardner, L.R., 2010. Contrasting lithium and magnesium isotope fractionation during continental weathering. Earth Planet. Sci. Lett. 300, 63–71. https://doi.org/10.1016/j.epsl.2010.09.036.

Teng, F.Z., Hu, Y., Ma, J.L., Wei, G.J., Rudnick, R.L., 2020. Potassium isotope fractionation during continental weathering and implications for global K isotopic balance. Geochim. Cosmochim. Acta 278, 261–271. https://doi.org/10.1016/j.gca.2020.02.029.

Thanh, L.D., Sprik, R., 2016. Zeta potential in porous rocks in contact with monovalent and divalent electrolyte aqueous solutions. Geophysics 81, D303–D314. https://doi.org/10.1190/GEO2015-0571.1.

Tomascak, P.B., Tera, F., Helz, R.T., Walker, R.J., 1999. The absence of lithium isotope fractionation during basalt differentiation: New measurements by multicollector sector ICP-MS. Geochim. Cosmochim. Acta 63, 907–910. https://doi.org/10.1016/S0016-7037(98)00318-4.

Tomascak, P.B., Magna, T., Dohmen, R., 2016. Advances in Lithium Isotope Geochemistry. Springer. https://doi.org/10.1007/978-3-319-01430-2.

Tuller-Ross, B., Savage, P.S., Chen, H., Wang, K., 2019. Potassium isotope fractionation during magmatic differentiation of basalt to rhyolite. Chem. Geol. 525, 37–45. https://doi.org/10.1016/j.chemgeo.2019.07.017.

Verney-Carron, A., Vigier, N., Millot, R., 2011. Experimental determination of the role of diffusion on Li isotope fractionation during basaltic glass weathering. Geochim. Cosmochim. Acta 75, 3452–3468. https://doi.org/10.1016/j.gca.2011.03.019.

Vigier, N., Decarreau, A., Millot, R., Carignan, J., Petit, S., France-Lanord, C., 2008. Quantifying Li isotope fractionation during smectite formation and implications for the Li cycle. Geochim. Cosmochim. Acta 72, 780–792. https://doi.org/10.1016/j.gca.2007.11.011.

Voegelin, A.R., Nägler, T.F., Pettke, T., Neubert, N., Steinmann, M., Pourret, O., Villa, I. M., 2012. The impact of igneous bedrock weathering on the Mo isotopic composition of stream waters: Natural samples and laboratory experiments. Geochim. Cosmochim. Acta 86, 150–165. https://doi.org/10.1016/j.gca.2012.02.029.

Wall, A.J., Mathur, R., Post, J.E., Heaney, P.J., 2011. Cu isotope fractionation during bornite dissolution: an in situ X-ray diffraction analysis. Ore Geol. Rev. 42, 62–70. https://doi.org/10.1016/j.oregeorev.2011.01.001.

Wang, K., Jacobsen, S.B., 2016. An estimate of the Bulk Silicate Earth potassium isotopic composition based on MC-ICPMS measurements of basalts. Geochim. Cosmochim. Acta 178, 223–232. https://doi.org/10.1016/j.gca.2015.12.039.

Wang, K., Peucker-Ehrenbrink, B., Chen, H., Lee, H., Hasenmueller, E.A., 2021. Dissolved potassium isotopic composition of major world rivers. Geochim. Cosmochim. Acta 294, 145–159. https://doi.org/10.1016/j.gca.2020.11.012.

Weiss, D.J., Boye, K., Caldelas, C., Fendorf, S., 2014. Zinc Isotope Fractionation during early Dissolution of Biotite Granite. Soil Sci. Soc. Am. J. 78, 171–179. https://doi.org/10.2136/sssaj2012.0426.

Weissbart, E.J., Rimstidt, J.D., 2000. Wollastonite: Incongruent dissolution and leached layer formation. Geochim. Cosmochim. Acta 64, 4007–4016. https://doi.org/10.1016/S0016-7037(00)00475-0.

Wetzel, F., de Souza, G.F., Reynolds, B.C., 2014. What controls silicon isotope fractionation during dissolution of diatom opal? Geochim. Cosmochim. Acta 131, 128–137. https://doi.org/10.1016/j.gca.2014.01.028.

Wiederhold, J.G., Kraemer, S.M., Teutsch, N., Borer, P.M., Halliday, A.N., Kretzschmar, R., 2006. Iron isotope fractionation during proton-promoted, ligand-controlled, and reductive dissolution of goethite. Environ. Sci. Technol. 40, 3787–3793. https://doi.org/10.1021/es052228y.

Williams, L.B., Hervig, R.L., 2005. Lithium and boron isotopes in illite-smectite: the importance of crystal size. Geochim. Cosmochim. Acta 69, 5705–5716. https://doi.org/10.1016/j.gca.2005.08.005.

Wimpenny, J., Gíslason, S.R., James, R.H., Gannoun, A., Pogge Von Strandmann, P.A.E., Burton, K.W., 2010. The behaviour of Li and Mg isotopes during primary phase dissolution and secondary mineral formation in basalt. Geochim. Cosmochim. Acta 74, 5259–5279. https://doi.org/10.1016/j.gca.2010.06.028.

Wimpenny, J., Colla, C.A., Yu, P., Yin, Q.Z., Rustad, J.R., Casey, W.H., 2015. Lithium isotope fractionation during uptake by gibbsite. Geochim. Cosmochim. Acta 168, 133–150. https://doi.org/10.1016/j.gca.2015.07.011.

Wunder, B., Meixner, A., Romer, R.L., Feenstra, A., Schettler, G., Heinrich, W., 2007. Lithium isotope fractionation between Li-bearing staurolite, Li-mica and aqueous fluids: an experimental study. Chem. Geol. 238, 277–290. https://doi.org/10.1016/j.chemgeo.2006.12.001.

Yamaguchi, T., Ohzono, H., Yamagami, M., Yamanaka, K., Yoshida, K., Wakita, H., 2010. Ion hydration in aqueous solutions of lithium chloride, nickel chloride, and caesium chloride in ambient to supercritical water. J. Mol. Liq. 153, 2–8. https://doi.org/10.1016/j.molliq.2009.10.012.

Yin, Z., Ding, Z., Hu, H., Liu, K., Chen, Q., 2010. Dissolution of zinc silicate (hemimorphite) with ammonia-ammonium chloride solution. Hydrometallurgy 103, 215–220. https://doi.org/10.1016/j.hydromet.2010.03.006.

Zeng, H., Rozsa, V.F., Nie, N.X., Zhang, Z., Pham, T.A., Galli, G., Dauphas, N., 2019. Ab initio calculation of equilibrium isotopic fractionations of potassium and rubidium in minerals and water. ACS Earth Space Chem. 3, 2601–2612. https://doi.org/10.1021/acsearthspacechem.9b00180.

Zhang, W., Qi, L., Hu, Z., Zheng, C., Liu, Y., Chen, H., Gao, S., Hu, S., 2016. An Investigation of digestion methods for trace elements in bauxite and their determination in ten bauxite reference materials using Inductively coupled plasma-mass spectrometry. Geostand. Geoanal. Res. 40, 195–216. https://doi.org/10.1111/j.1751-908X.2015.00356.x.

Zhao, M.Y., Zheng, Y.F., 2015. The intensity of chemical weathering: Geochemical constraints from marine detrital sediments of Triassic age in South China. Chem. Geol. 391, 111–122. https://doi.org/10.1016/j.chemgeo.2014.11.004.